LASER WRITING OF THE ELECTRONIC ACTIVITY OF NITROGEN AND HYDROGEN ATOMS IN GALLIUM ARSENIDE

Nilanthy Balakrishnan, BSc (Hons) in Physics.

Dissertation Submitted to the University of Nottingham

for the degree of Master by Research in Physics

September 2011

UNIVERSITY OF NOTTINGHAM

Abstract

Faculty of Science

School of Physics and Astronomy

Master by Research in Physics

by Nilanthy Balakrishnan, BSc (Hons) in Physics

In this study, we use a focussed laser beam to control the electronic activity of N- and H-atoms in a dilute nitride Ga(AsN)/GaAs quantum well (QW). We find that the laser can be used to dissociate N-H complexes in hydrogenated Ga(AsN) thus enabling us to control the photoluminescence emission energy of the QW with submicron spatial resolution. The mechanism responsible for the dissociation results from the combination of thermal heating and photoexcitation phenomena.

The H-distribution profile across the laser annealed region is probed by secondary electron imaging in a field-emission scanning electron microscope. The spatial distribution of H inside the annealed region is characterized by an inverted Gaussian with a minimum corresponding to a lower H-content.

Our laser writing approach yields sub-micron resolution in the spatial manipulation of the electronic properties and can provide an alternative method to masking techniques for H-defect engineering and in-plane patterning of the band gap energy of interest for new nanotechnologies.

List of Publications

N. Balakrishnan, A. Patanè, O. Makarovsky, A. Polimeni, M. Capizzi, F. Martelli and S. Rubini. Laser writing of the electronic activity of N- and H-atoms in GaAs. *Applied Physics Letters* **99**, 021105 (2011).

Acknowledgements

First of all, I wish to express my heartfelt thanks to my supervisor, Prof. Amalia Patanè, for providing me with the opportunity to work under her supervision, guiding me throughout this research work, and giving valuable advices and encouragement, which allowed me to carry out this MSc by Research.

Secondly, my thanks go to Dr. Oleg Makarovsky for his support in the laboratory and fruitful discussions in planning experiments, interpreting results and theoretical modelling.

I would also like to express my thanks to Dr. Michael Fay for his assistance in the SEM experiments and to Dr. Lyudmila Turyanska for her guidance and help in the AFM studies.

I am grateful to Prof. A. Polimeni and Prof. M. Capizzi (The University of Rome, Italy) and Dr. F. Martelli and Dr. S. Rubini (TASC-INFM-CNR, Italy) for providing samples for this research study, and for their contribution to our join publication in Applied Physics Letters.

I acknowledge The Royal Society, The University of Nottingham and the COST Action MP0805 for funding this research work.

My special thanks go to my colleagues for their moral supports and providing a fantastic year in my life.

My deepest thank goes to my family members, relatives and friends for their encouragement to undertake this Master degree in the UK.

Abbreviations

AFM	**A**tomic **F**orce **M**icroscopy
BAC	**B**and **A**nti**c**rossing
CB	**C**onduction **B**and
CL	**C**athodo**l**uminescence
FE	**F**ree **E**xciton
HMA	**H**ighly **M**ismatched **A**lloy
HR	**H**igh **R**esolution
HRXRD	**H**igh **R**esolution **X**-**R**ay **D**iffraction
IR	**I**nfra**r**ed
LCINS	**L**inear **C**ombination of **I**solated **N**itrogen **R**esonant **S**tates
LDA	**L**ocal **D**ensity functional **A**pproximation
LED	**L**ight **E**mitting **D**iode
MBE	**M**olecular **B**eam **E**pitaxy
OD	**O**ptical **D**ensity
PL	**P**hoto**l**uminescence
QW	**Q**uantum **W**ell
SE	**S**econdary **E**lectron
SEM	**S**canning **E**lectron **M**icroscopy
TB	**T**ight **B**inding
TEM	**T**ransmission **E**lectron **M**icroscopy
UV	**U**ltra**v**iolet
VB	**V**alence **B**and

Physical Constants

Quantity	Symbol	Value	Unit
Boltzmann constant	k_B	1.38065×10^{-23}	JK^{-1}
Electron charge	e	1.60218×10^{-19}	C
Electron rest mass	m_0	9.10938×10^{-31}	kg
Permittivity in vacuum	ε_0	8.85419×10^{-12}	Fm^{-1}
Plank constant	h	6.62617×10^{-34}	Js
Reduced Plank constant ($h/2\pi$)	$\hbar$	1.05458×10^{-34}	Js
Speed of light in vacuum	c	2.99792×10^{8}	ms^{-1}

List of Figures

List of Tables

List of Contents

Chapter 1

Introduction

The incorporation of a small concentration (~1%) of N-atoms onto the anion sublattice of a III-V crystal induces a large reduction of the band gap energy [1-2] and an unusual response to external perturbations, such as hydrostatic pressure [1]. On the other hand, H-atoms are highly mobile and reactive elements that passivate both deep and shallow crystal defects and impurities in semiconductors [3-4]. In particular, the incorporation of hydrogen in III-N-Vs acts to neutralize the electronic activity of nitrogen through the formation of N-H complexes, thus reversing the effect of the N-atoms on the band structure of the host crystal [5-7]. Recently, thermal annealing [8-10] and masking techniques [7, 11] were used to dissociate N-H complexes, thus enabling the control of the band gap energy of Ga(AsN) with sub-micron spatial resolution.

This dissertation presents a novel technique and physical mechanism that enable a similar control. We control the electronic activity of N- and H-atoms in a Ga(AsN)/GaAs quantum well (QW) using a focussed laser beam. Our laser writing technique and micro-photoluminescence (μPL) studies provide real-time *in-situ* characterisation and control of the N-H complex dissociation and of the band gap energy of Ga(AsN). This technique yields sub-micron resolution in the spatial manipulation of the electronic properties and could provide an alternative route to masking methods for H-defect engineering and

in-plane patterning of the band gap energy [7, 11] for nanophotonics [12] and photovoltaics [13].

This dissertation is structured as follows. Chapter 2 discusses the effect of N- and H-atoms on the electronic properties of GaAs and includes a detailed description of N-induced compositional fluctuations, N-pairs and clusters, and N-H complexes in GaAs.

Chapter 3 provides a brief overview of the sample growth, the hydrogenation technique, and experimental apparatus.

Chapter 4 introduces the laser writing and thermal annealing studies. Light emitting sub-micron spots are produced by laser writing with different exposure conditions (time and/or power) and the thermal stability of these spots are investigated. Activation energies for the N-H complex dissociation by both laser and thermal annealing are determined.

Chapter 5 presents the compositional and topographical studies of the laser annealed regions. The H-distribution profile across a laser annealed line is probed using secondary electron (SE) imaging in scanning electron microscopy (SEM). This profile is modelled using Fick's equation for H diffusion in one dimension.

Chapter 6 describes the low temperature and temperature dependent PL studies of an hydrogenated Ga(AsN) quantum well (QW). Energy levels of N-pairs are identified. An unusual S-shaped temperature dependence of the QW peak energy is also described.

Chapter 7 concludes this dissertation by providing a summary of the main findings and a proposal for future studies.

This dissertation contains two appendixes. Appendix A describes the derivation of the dependence of the electron effective mass of $GaAs_{1-x}N_x$ on the N-content, x. Appendix B describes the electronic bound states of a Ga(AsN)/GaAs QW using the band anticrossing (BAC) model and a QW square potential model.

Chapter 2

Effect of N- and H-Atoms on the Electronic Properties of GaAs

The controlled incorporation of impurities in a semiconductor crystal during or after the synthesis is routinely used to tailor electronic properties and has played a key role in the discovery of physical phenomena and their exploitation in device applications. Among various elements, nitrogen and hydrogen in III-V compounds have revealed intriguing effects of fundamental interest and technological importance. In this chapter we discuss the unique effect of nitrogen (N) and hydrogen (H) atoms on the electronic properties of GaAs.

2.1 Nitrogen incorporation in GaAs

During the last decade, III-V-N alloys such as $In_yGa_{1-y}As_{1-x}N_x$, $GaP_{1-x}N_x$ and $GaAs_{1-x}N_x$ have received considerable attention due to their unique electronic properties and useful applications in optoelectronic devices [14]. In these alloys, the group V anions are partially substituted by a low concentration of highly electronegative N atoms [15] (see Figure 2.1a). In general, a smaller lattice constant increases the band gap; however, nitrogen causes a giant band gap bowing and tends to stretch and compress the neighbouring bonds [16], see Figure 2.1b. Moreover, a small amount (~ 1%) of N in III-Vs produces a considerable decrease in the electron mobility [17], an increase of the electron effective mass [18] and an unusual response to external perturbations, such as

hydrostatic pressure [1]. Many of these effects can be explained by a two-level band anticrossing (BAC) model in which the extended conduction band (CB) states of GaAs admix and hybridize with the localized N-level above the CB edge [1]. This model is described in the following section.

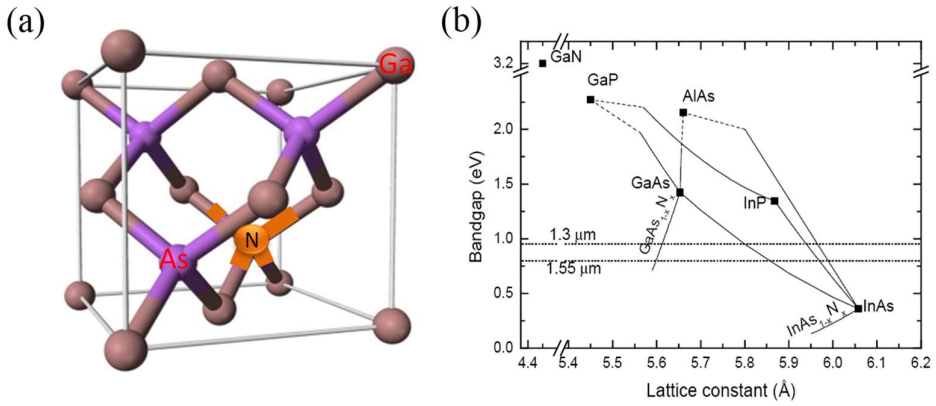

Figure 2.1: (a) Unit cell of GaAs in which an As-atom is replaced by a N-atom to form Ga(AsN). (b) Dependence of the band gap energy on the lattice constant for III-V semiconductors. The solid and dashed lines are, respectively, the ternary compounds' direct and indirect band gaps. The horizontal lines represent fiber-optical communication wavelengths (1.55 and 1.3 µm). Picture (b) reproduced from Ref [16].

2.1.1 Band anticrossing model of the dilute nitride Ga(AsN) alloy

The unexpected red shift of the photoluminescence (PL) of the dilute Ga(AsN) alloy, instead of a blue shift, was firstly reported by M. Weyers et al. [19]. This discovery has opened an important question about the physical mechanism responsible for this unusual behaviour. S. Wei and A. Zunger [20] have explained the origin of this red shift and corresponding band gap reduction in terms of an optical bowing parameter which is largely dependent on the N-content. On the other hand, the two-level BAC model has explained the behaviour of many highly mismatched alloys (HMAs) and was originally

developed by W. Shan et al. [1] to describe the dependence of the band gap on composition and pressure for the $In_yGa_{1-y}As_{1-x}N_x$ alloy. The BAC model has predicted many interesting effects, such as an enhancement of the donor binding energy [21] and electron effective mass [17] due to N incorporation, which have been experimentally proved.

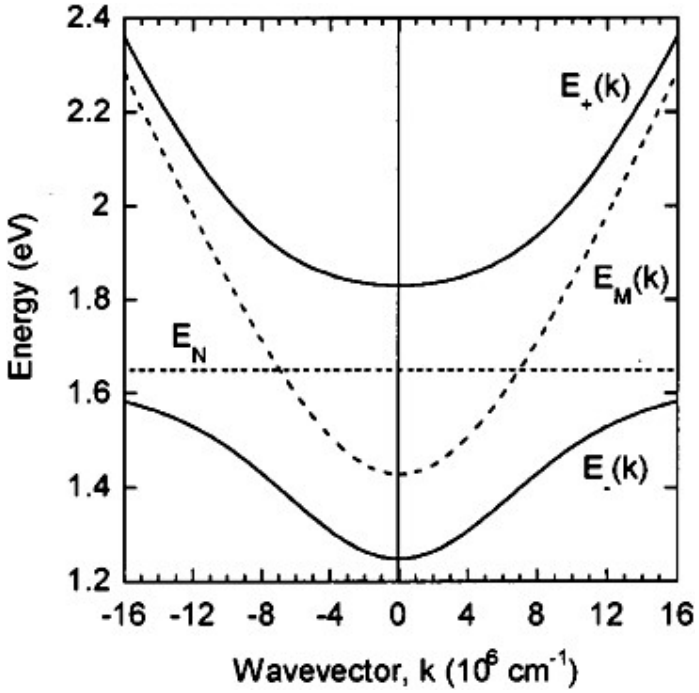

Figure 2.2: Solid lines: calculated dispersion relationships for $E_{\pm}$ subbands of $GaAs_{0.99}N_{0.01}$ using the BAC model. Dashed lines: unperturbed energies of the N level (E_N) and the GaAs conduction band. Picture reproduced from Ref [18].

The two-level BAC model is the solution of the degenerate perturbation theory applied to a system of localized and extended states, see Figure 2.2. Following W. Walukiewicz et al. [22], the interaction between these two types of states leads to the following eigenvalue problem

$$\begin{vmatrix} E(k) - E_M(k) & V_{MN} \\ V_{MN} & E(k) - E_N \end{vmatrix} = 0\,, \qquad (2.1)$$

where $E_M(k)$ and E_N are, respectively, the energies of the GaAs CB host matrix and of the N level measured with respect to the top of the valence band (VB), $V_{MN} = \langle k|\mathrm{V}|\mathrm{N}\rangle$ is the matrix element describing the interaction between the localized N states and extended CB states, and V is the potential generated by a single N-atom on a substitutional site. The two possible solutions of this problem can be written as

$$E_{\pm}(k) = \frac{1}{2}\left\{\left(E_N + E_M(k)\right) \pm \sqrt{\left[\left(E_N - E_M(k)\right)^2 + 4{V_{MN}}^2\right]}\right\}. \quad (2.2)$$

If we assume that V_{MN} is independent of k near the CB edge, then V_{MN} can be written as

$$V_{MN} = C_{MN}x^{1/2}\,, \quad (2.3)$$

where C_{MN} is a constant dependent on the host matrix and x is the mole fraction of substitutional N. Therefore Eq. 2.2 can be also rewritten as

$$E_{\pm}(k) = \frac{1}{2}\left\{(E_N + E_M(k)) \pm \sqrt{\left[(E_N - E_M(k))^2 + 4{C_{MN}}^2 x\right]}\right\}. \quad (2.4)$$

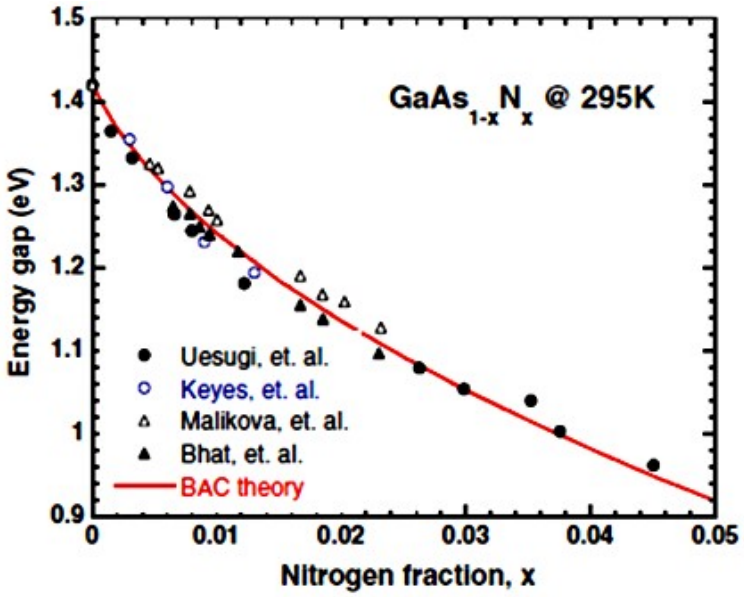

Figure 2.3: Dependence of the band gap energy of $GaAs_{1-x}N_x$ on x reported by different groups. The solid line is the best fit to the data with C_{MN} = 2.7 eV. Picture reproduced from Ref. [15].

Figure 2.2 shows the energy dispersion $E(k)$ relation for the $E_{\pm}$ subbands. Figure 2.3 illustrates the dependence of the band gap energy of $GaAs_{1-x}N_x$ on x reported by different research groups, and the fit to the data by the BAC model with a coupling constant C_{MN} = 2.7 eV [15] and a N-level E_N = 1.65 eV [1, 21-24].

2.1.2 Electron effective mass in Ga(AsN)

The incorporation of N in GaAs not only changes the band gap energy, but also it modifies the curvature of the energy-wave vector $E(k)$ dispersion of the conduction band, thus changing the electron effective mass m^*. The second derivative effective mass, m^*, can be written as

$$m^*(k) = \frac{\hbar^2}{d^2E(k)/dk^2}. \tag{2.5}$$

Using Eq. 2.5 and the k-dependence of the $E_-(k)$ subband in Eq. 2.4, we find that for Ga(AsN) the effective mass at $k = 0$ can be expressed as

$$m^* = \frac{2m_0^*}{\left[1 - \frac{(E_N - E_M(k))}{\sqrt{(E_N - E_M(k))^2 + 4C_{MN}^2 x}}\right]}, \tag{2.6}$$

where m_0^* is the electron effective mass in GaAs. For the derivation of Eq. 2.6, see Appendix A.

Figure 2.4 shows the dependence of m^* on x. In this Figure the value of m^* is normalized to the value of the electron mass in vacuum (m_0).

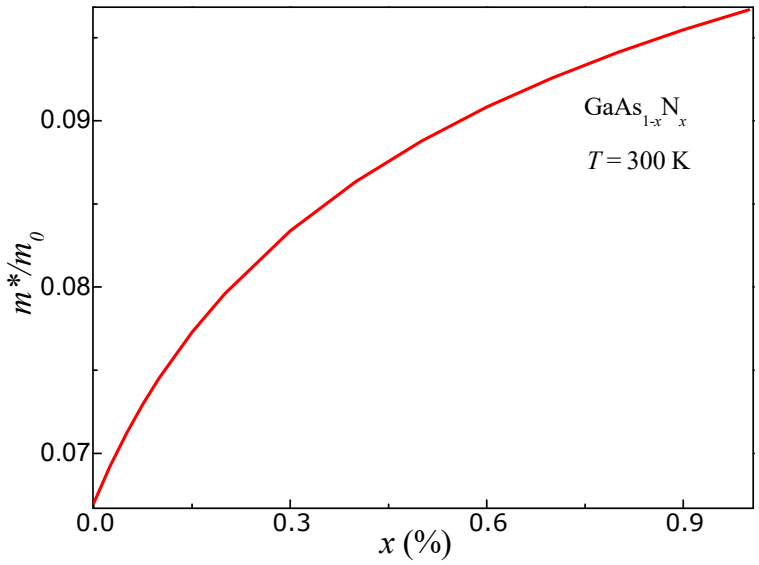

Figure 2.4: Dependence of the electron effective mass on x in $GaAs_{1-x}N_x$ calculated using the BAC model at T = 300 K (E_N = 1.65 eV, $E_M(k = 0)$ = 1.424 eV [25], C_{MN} = 2.7 eV and $m_0^* = 0.067\ m_0$).

2.1.3 $GaAs_{1-x}N_x$/GaAs quantum wells

In this section we describe the electronic bound states of a Ga(AsN)/GaAs QW using the BAC model and a QW square potential model. The height of the QW is $V_0 = E_g(GaAs) - E_g(GaAs_{1-x}N_x)$ where E_g is the band gap energy. The potential profile along the growth direction z is given by

$$V(z) = \begin{cases} V_0 & |z| > \frac{a}{2} \\ 0 & |z| < \frac{a}{2} \end{cases}, \qquad (2.7)$$

where a is the width of the QW centred at z = 0.

The wave functions inside the well have even/odd symmetry and can be written as $\psi(z) = C\begin{cases}\cos kz \\ \sin kz\end{cases}$, where $\varepsilon = \frac{\hbar^2 k^2}{2m_w^*}$ and m_w^* is the electron effective mass inside the well.

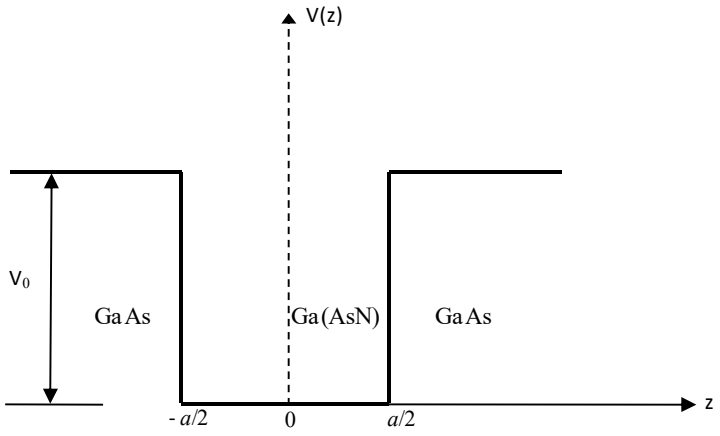

Figure 2.5: Schematic diagram of a finite square Ga(AsN)/GaAs QW.

Outside the well, $\psi(\mathrm{z}) = D\exp(\pm K\mathrm{z})$, $\varepsilon = \mathrm{V}_0 - \frac{\hbar^2 K^2}{2m_b^*}$ and m_b^* is the electron effective mass outside the well. Hence the energy of the transition between the first QW electron subband ε_1 and the top of the valence band is

$$E_{QW} = E_g + \varepsilon_1, \tag{2.8}$$

where E_g is the band gap energy of Ga(AsN). The value of E_{QW} is affected by the Coulomb interaction between electrons and holes and is decreased by a small amount due to the exciton binding energy. In the discussions that follow we will neglect this small correction (< 5 meV) to the value of E_{QW}.

Figure 2.6 shows the dependence on x of E_g and E_{QW} for a QW of width a = 6 nm. For the derivation of Eq. 2.8 and the values of E_{QW} in Figure 2.6, see Appendix B. We note that the ground state electron energy ε_1 is inversely proportional to the electron effective mass in $GaAs_{1-x}N_x$. However, despite the electron mass increases with x, ε_1 does not decrease. This is due to the dominant increase of the QW potential height V_0 with increasing x, thus leading to a larger value of ε_1.

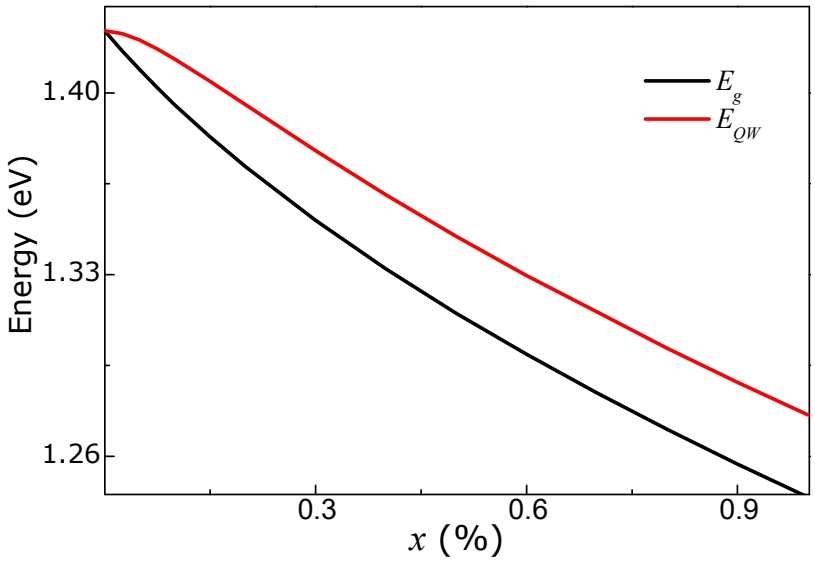

Figure 2.6: Dependence on x of the band gap energy of $GaAs_{1-x}N_x$ (E_g) and of the inter band transition energy of a Ga(AsN)/GaAs QW with a = 6 nm (T = 300 K).

2.1.4 Compositional fluctuations in semiconductor alloys

Compositional fluctuations in an alloy lead to a spatially varying potential and potential minima that can localize excitons. In turn this can lead to a statistical distribution of excitonic emission lines and a broadening of the optical spectra [26]. According to a simple model of exciton thermalization in a disordered potential, the photoluminescence (PL) peak position is red-shifted compared to the absorption peak by an amount (Stokes shift) given by $-\sigma_E^2/k_BT$, where σ_E is the standard deviation of the absorption line [26-27]. On the other hand the temperature dependence of the band gap energy is described by the Varshni law

$$E_g(T) = E_g(0\text{ K}) - \frac{\alpha T^2}{T+\beta}, \tag{2.9}$$

where $E_g(0\text{ K})$ is the band gap at T = 0 K, and α and β are fitting parameters

[28]. Hence taking into account the Stokes shift, we can describe the *T*-dependence of the PL energy as

$$E_g(T) = E_g(0\ \mathrm{K}) - \frac{\alpha T^2}{T+\beta} - \frac{\sigma_E{}^2}{k_B T}. \qquad (2.10)$$

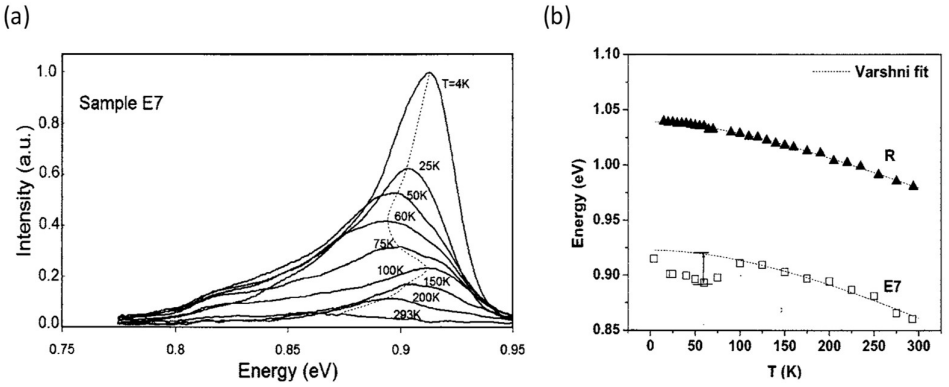

Figure 2.7: (a) PL spectra of a GaAsSbN/GaAs QW (sample E7), the dotted line is a guide to the eye. (b) Dependence of the PL peak energy on temperature for a GaAsSb/GaAs QW (sample R) and a GaAsSbN/GaAs QW (sample E7). The dotted lines are the Varshni fits. Pictures reproduced from Ref. [29].

According to Eq. 2.10, the values of E_g can exhibit a non-monotonic dependence on *T* and can either decrease or increase with increasing *T*. A more complicated scenario can occur if excitons cannot thermalize. At low temperatures, for k_BT small compared to the height of the fluctuating potential barriers, the excitons remain trapped in local energy minima and cannot thermalize. Eq. 2.10 no longer describes the *T*-dependence of the PL energy. In this case, the peak position remains fixed or show a non-monotonic and complicated *T*-dependence [26] as shown in Figure 2.7a for a GaAsSbN QW (sample E7) [29]. The QW PL peak position shows a red-blue-red shift. In contrast, the QW PL peak energy of GaAsSb (sample R) is well described by the Varshni law.

Alloy compositional fluctuations can also cause anisotropic PL line shapes with a low energy PL tail due to recombination of excitons on localized states at low temperatures [30]. Theoretical studies report that the density of states associated with this tail, g($h\upsilon$), can be written as

$$g(h\upsilon) = g_0 \exp\left\{-[(h\upsilon - h\upsilon_{exc})/\varepsilon_0]^{3/2}\right\}, \quad (2.11)$$

where g_0 is a constant, $h\upsilon_{exc}$ is the recombination energy of the free exciton (FE), and ε_0 is a characteristic energy [30-32]. The PL line shape, I($h\upsilon$), is then given by

$$I(h\upsilon) = \beta\, n_0\, g(h\upsilon)\, \tau(h\upsilon)\, \tau_R^{-1} \exp[\Gamma(h\upsilon)], \quad (2.12)$$

where β is the coefficient that describes the capture of the FE into the localized states, $\Gamma(h\upsilon)$ is a function of the localized energy $h\upsilon$, and $\tau(h\upsilon)$ is the lifetime of the localized exciton given by

$$\tau^{-1}(h\upsilon) = \tau_R^{-1}\{1+\exp[\delta\,(h\upsilon_m - h\upsilon)]\}. \quad (2.13)$$

Here τ_R is the radiative lifetime and δ and $h\upsilon_m$ are phenomenological parameters [30-32]. The PL spectra (open circle) for an InGaAsN QW at T = 10 K is shown in Figure 2.8. The solid line is the fit to the data using Eq. 2.13.

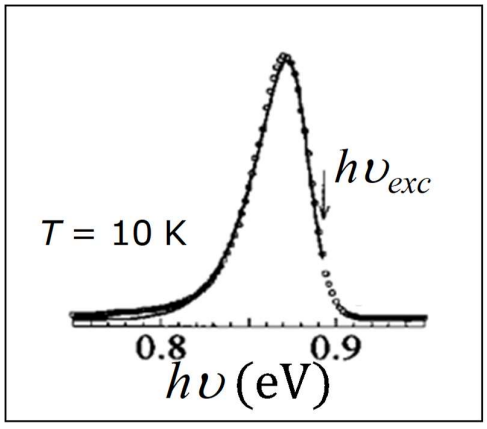

Figure 2.8: Low temperature PL spectrum of an $In_{0.38}Ga_{0.62}As_{0.978}N_{0.022}$/GaAs QW (open circle). The solid line is a fit to the data, as discussed in the text. $h\upsilon_{exc}$ is the free exciton energy. Picture reproduced from Ref [32].

2.1.5 Nitrogen pairs and clusters in GaAs

In III-V-N alloys, the BAC model describes well the variation of the subband energies, E_+ and E_-, with the nitrogen content, x. However, it omits many interesting effects of the N on the band structure. A series of nitrogen related energy states can be found close to E_- and E_+ [33] due to the formation of N pairs and clusters [33]. Pair of N-atoms can replace an As-atom in GaAs to form isoelectronic traps, whose binding energy varies with increasing the distance between the N-atoms [34]. Interestingly, the pair induced states in the band gap vary non-monotonically with the separation between the N-atoms [33].

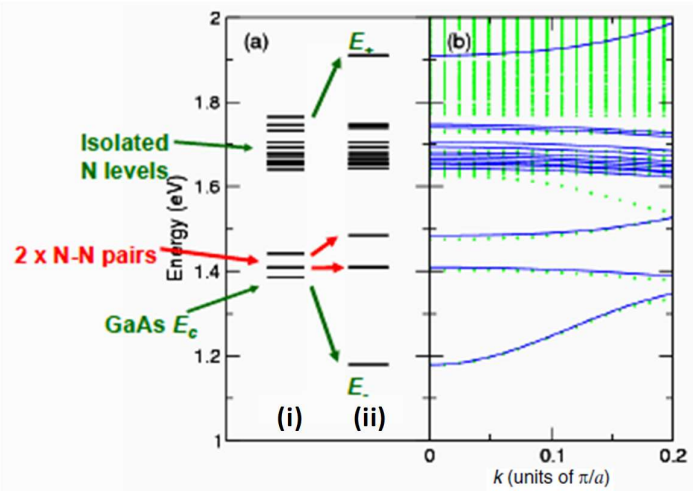

Figure 2.9: (a) Calculated N-cluster state energies and CB for a $Ga_{500}As_{487}N_{13}$ supercell (i) before and (ii) after inclusion of the interaction of the N-levels with the CB states of GaAs. (b) Supercell band dispersion derived from the TB (dotted lines) and LCINS models (solid lines). Picture reproduced from Ref [2].

A. Lindsay and E. P. O'Reilly [2] determined the energy levels of N related states in Ga(AsN) using the tight-binding (TB) method and described the CB by using the linear combination of isolated nitrogen resonant states

(LCINS) model. In this model, the hybridization and admixing of the CB states and the sequence of localized N-related states in the CB leads to a complex band structure. Figure 2.9a shows the energy of the N and CB edge states for a $Ga_{500}As_{487}N_{13}$ supercell without (i) and with (ii) the inclusion of the coupling between the two set of states. The dotted lines in Figure 2.9b show the band dispersion calculated using the TB method. The solid lines show the CB dispersions calculated using the LCINS model. Both models, TB and LICNS, produce similar results and reveal non-parabolic dispersion and strongly admixed states [2].

2.2 Hydrogen in Ga(AsN)

The unavoidable presence of hydrogen during the sample growth and/or device processing steps, has stimulated a great interest in the effects of H in semiconductor compounds [35]. H-atoms are highly mobile and reactive elements that passivate both deep and shallow crystal defects and impurities in semiconductors [3-4]. In particular, the incorporation of H in III-N-Vs acts to neutralize the electronic activity of N through the formation of N-H complexes, thus reversing the effect of the N-atoms on the band structure of the host crystal [5-7]. Moreover, H turns the tensile strain of Ga(AsN) into compressive and induces an expansion of the lattice constant, which can become larger than that of GaAs [36-37]. This section reviews the recent literature on N-H complexes.

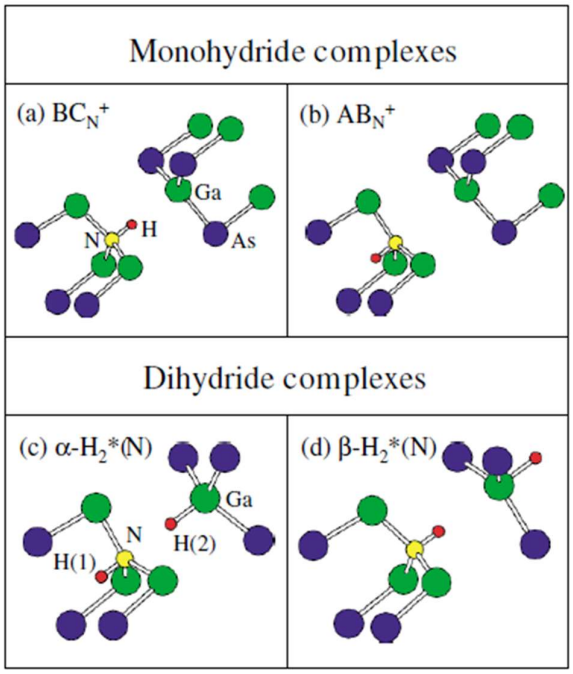

Figure 2.10: Models of possible N-H complexes in Ga(AsN). Single H at the (a) bond centre site next to N (BC_N), and (b) antibonding site (AB_N). Dihydrogen complexes (c) α-H_2*(N) and (d) β-H_2*(N). Picture reproduced from Ref [39].

Theoretical studies based on the local density functional approximation (LDA) in Ga(AsN) supercells have indicated a variety of possible N-H complexes in GaAs [38-40], as shown in Figure 2.10. In all configurations the N-H bond length is equal to 1.05 Å [39], and N and Ga atoms are moved outward from their basal plane [38-39]. In the configurations BC_N^+ and AB_N^+, the H is bonded to a N-atom at the bond centre and antibonding site, respectively, [38-39] with a separation between the H and Ga atoms of 2.41 Å [39]. The positive sign indicates the charge state of the monohydride configuration. In the configuration α-H_2*(N), an H-atom (H(1)) is bonded to the N-atom at the antibonding site and the second H-atom (H(2)) is bonded to the Ga-atom at the bond centre site. The Ga-H bond length is equal to 1.54 Å. No chemical bond is established between the N and H(2) atoms [39]. The same

applies to the β-H_2*(N) configuration, except that the Ga-H bond length is equal to 1.60 Å [39].

The formation of mono and dihydrogen complexes depends on the position of the Fermi level in the alloy [38-40]. A *p*-type doping tends to favour the monohydrogen complexes, whereas *n*-type doping favours dihydrogen complexes [38, 40]. Also, low H-concentrations favour monohydrogen complexes and high concentration of H are likely to form dihydrogen complexes [38, 40]. Interestingly, monohydrogen complexes do not passivate the effect of N, but dihydrogen complexes do [38-40]. Monoatomic H is expected to behave as a donor in the undoped dilute Ga(AsN) alloy [39]. In contrast, dihydrogens should passivate the electronic activity of N thus recovering the electronic properties of GaAs [38-40].

Infrared absorption spectroscopy studies have suggested a model of trigonal H-N-H complex with two H atoms bonded with a N atom (see figure 2.11a). Theoretical calculations in Ref [40-42] have shown that this complex is unstable and easily transforms into the α-H_2*(N) complex. However, infrared absorption studies have demonstrate the existence of two weakly coupled N-H stretching modes and no modes related to the Ga-H bond [41-42]. This controversy was resolved in a latest theoretical study suggesting a different model for H-N-H complexes with C_{1h} symmetry [42], as shown in Figure (2.11b). Also, recent measurements of x-ray absorption and theory proposed a H-N-H complex with a C_{2v} or asymmetric C_{2v} configuration [42-43] (see Figure 2.11c and d). Both studies have not provided any evidence for the H_2*(N) configurations [42].

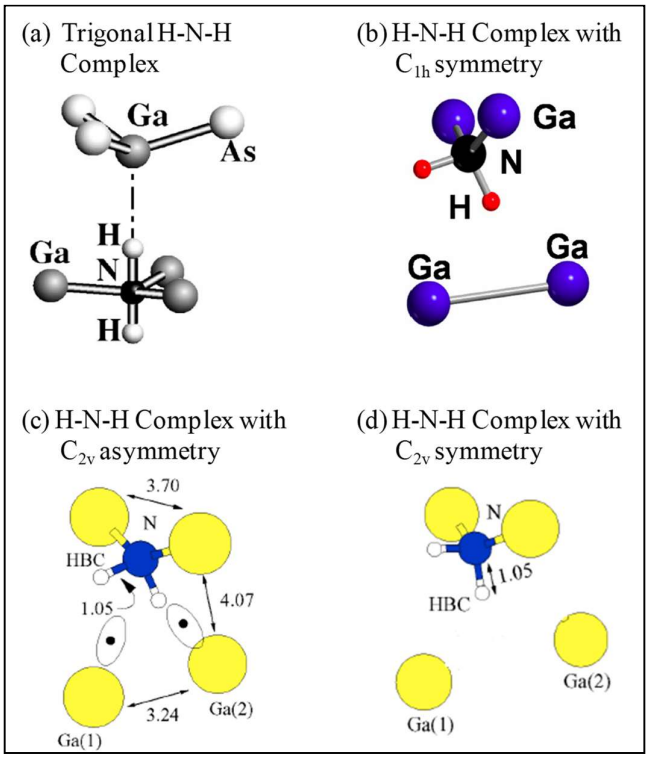

Figure 2.11: Configuration of the H-N-H complex: (a) trigonal, (b) with C_{1h} symmetry, (c) with C_{2v} asymmetry and (d) with C_{2v} symmetry. Pictures reproduced from Ref [40, 42-43].

As shown in Figure 2.11a, in the trigonal H-N-H complex, two hydrogen atoms are bonded to the same N atom [42]. The H-N-H complex with, respectively, C_{1h} symmetry, C_{2v} asymmetry and C_{2v} symmetry are shown in Figures 2.11b-d. In these three configurations the H breaks two Ga-N bonds and form N-H bonds. This also induces a dangling bond on each broken bond with Ga [42-43]. Recent experiments and theories have shown that the H-N-H complexes with C_{1h} symmetry and C_{2v} asymmetry can fully neutralize the electronic activity of the N atoms [9, 43-44]. Measurements of high resolution x-ray diffraction also suggested a third H atom is weakly trapped close to the H-N-H complex thus leading to compressive strain in Ga(AsN) [9, 44]. Thermal annealing at 250 °C removes this third H atom from the complex and

recovers the tensile strain, without changing the N-passivation effect [8-9]. At temperature around 330 °C, the H-N-H complex dissociates and N becomes electrically active [8-9]. These effects will be discussed later in the context of our laser writing experiments in hydrogenated Ga(AsN).

Chapter 3

Samples and Experimental Setup

This chapter describes the samples, experimental equipments and techniques used to obtain the results presented in this dissertation. This chapter is organized as follow. Section 3.1 describes the sample structure and growth conditions. Sections 3.2 - 3.4 illustrate the experimental equipments used for PL measurements. Section 3.5 describes the experimental setup for laser annealing. Finally, sections 3.6 and 3.7 present the experimental setup for compositional and topographical studies.

3.1 Sample growth and hydrogenation

In this study, we use a Ga(AsN)/GaAs QW sample. This was grown by Molecular Beam Epitaxy (MBE) on a (001)-oriented GaAs substrate. This structure has the following layer composition, in order of growth: an undoped GaAs buffer layer grown at 600 °C, a 6 nm Ga(AsN) (N = 0.9%) QW and a 30 nm undoped GaAs cap layer both grown at 500 °C. The N-content was determined by high resolution x-ray diffraction (HRXRD) measurements and further supported by PL studies showing that the Ga(AsN) QW PL emission is red-shifted by 0.13 eV relative to the GaAs PL emission at $T = 300$ K.

The as-grown sample was hydrogenated by ion beam irradiation using a Kaufman source. The hydrogenation was performed at 300 °C with an ion-beam energy of 100 eV and H-doses of $4x10^{16}$, $6x10^{16}$ and $8x10^{16}$ ions/cm^2.

We refer to these hydrogenated samples as H1, H2 and H3, respectively, and the non-hydrogenated sample as V. Also, an additional sample (H0) was considered. This was grown by MBE and has the same structure as sample V except for an additional $Al_{0.7}Ga_{0.3}As$ layer grown above the GaAs buffer layer and for the N content (1%) in the QW. This sample was hydrogenated with a H dose of $2x10^{16}$ ions/cm^2. The H dose for each sample is indicated in Table 3.1.

Table 3.1: H dose in samples V, H1, H2, H3, and H0.

Sample	*H dose* (ions/cm^2)
V	0
H1	$4x10^{16}$
H2	$6x10^{16}$
H3	$8x10^{16}$
H0	$2x10^{16}$

Figure 3.1a shows the detailed schematic diagram of a Kauffmann source. In the ionization chamber, the heated cathode filament provides an electron beam to ionize the H-plasma, which is magnetically confined. The H^+ ion beam is accelerated through the grid accelerator and impinges on the sample, which is mounted on the sample holder in the main chamber. The heating lamp behind the sample holder provides a constant temperature to the sample. This allows us to control the hydrogen diffusion depth profile. Figure 3.1b shows the Ga(AsN) QW structure and H diffusion along the growth direction z. The H tends to accumulate on the surface, but for sufficiently high temperatures, it can also diffuse into the bulk.

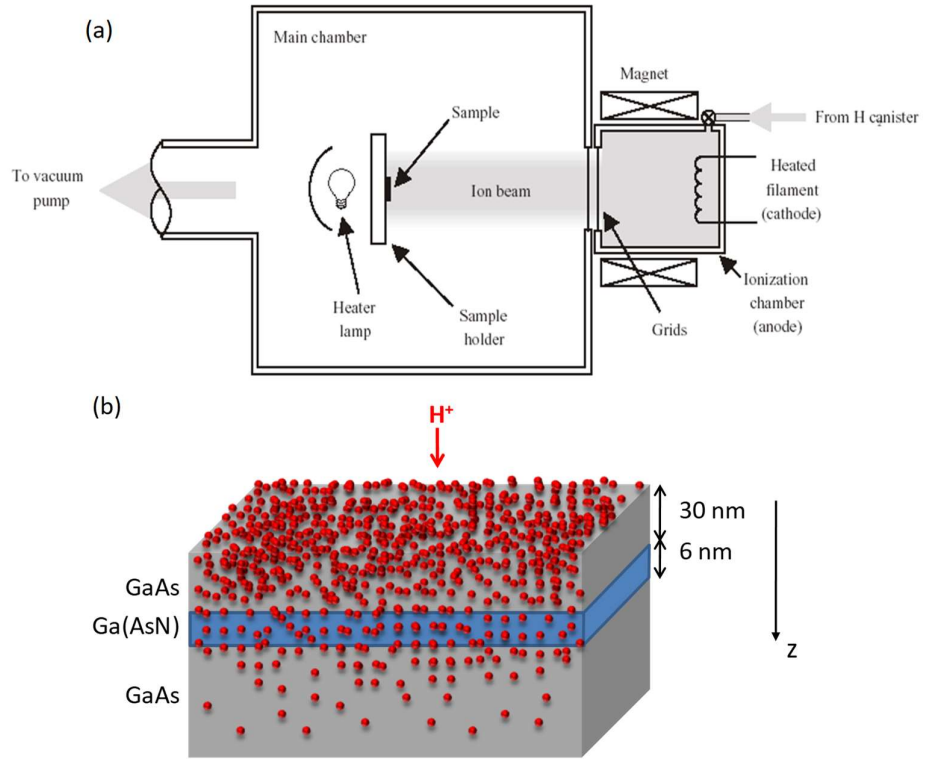

Figure 3.1: Schematic diagram of a Kaufmann source (a) and H-diffusion in a Ga(AsN)/GaAs QW (b).

3.2 Room temperature micro-photoluminescence

The room temperature μPL measurements were carried out using a LabRAM HR-UV spectrometer equipped with a confocal microscope. This system provides high optical resolution down to $\Delta\lambda = 10^{-2}$ nm. The schematic diagram of the system is shown in Figure 3.2. The system has four main parts, which are described below.

Optical Microscope: imaging is carried out via a standard optical microscope. This has 3 objectives that provide 10×, 50× and 100× magnification. The focal length (f) and numerical aperture (NA) of each objective are f = 18, 3.6, 1.8 mm and NA = 0.25, 0.55, 0.9, respectively.

Spectrometer: the μPL signal is dispersed by a grating and detected by an (InGa)As or a Si-CCD array photodiode. The (InGa)As detector covers the λ range 800 nm to 1600 nm and the Si-CCD detector covers the near UV to the visible range (350 nm to 800 nm). Two gratings (150 and 1200 g/mm) can be selected for measurements in different λ range and spectral resolution.

Optics: mirrors, beam splitter and filters are used to direct the laser beam from a He-Ne laser to the sample and for collecting light from the sample to the detectors.

XY/Z motorized stage: the stage can be moved point by point with a spatial resolution of 0.1μm along the X, Y and Z direction for area (X and Y) mapping, and line (X or Y) and depth (Z) profiling of the μPL. Mapping of the μPL along X and Y can also be carried out by scanning the laser over the fixed stage. This can be done by a motorized mirror.

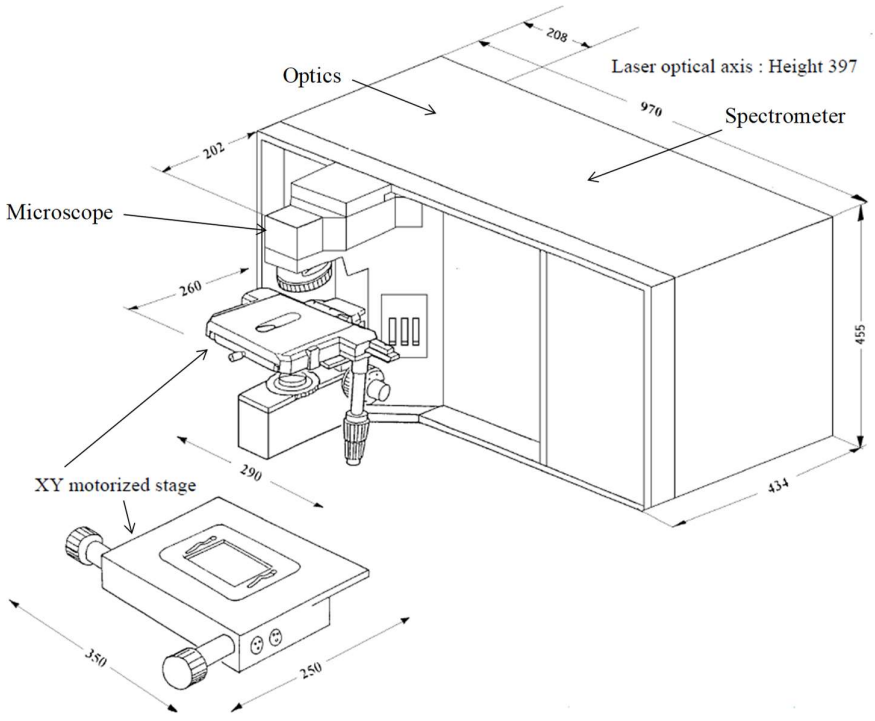

Figure 3.2: Schematic diagram of the LabRAM HR-UV Spectrometer. Diagram reproduced from Ref [45].

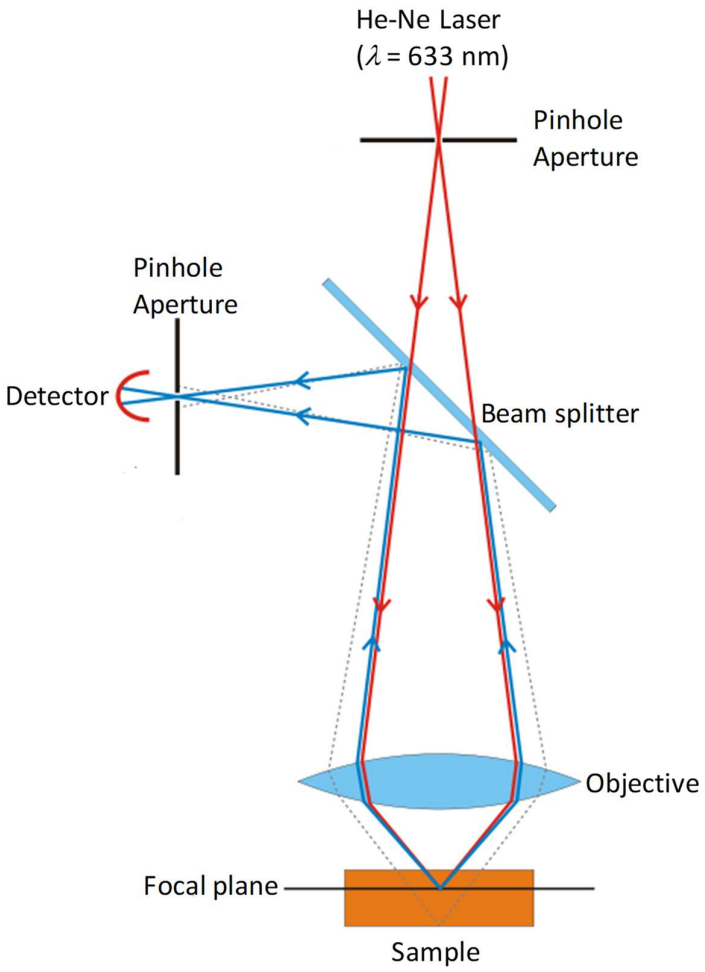

Figure 3.3: Schematic diagram of a confocal microscope. Picture reproduced from Ref [46].

The schematic diagram of a confocal microscope is shown in Figure 3.3. The laser beam is focused by an objective to a small, nearly diffraction-limited spot on the sample surface. Also, the same objective collects the photo-excited light from the sample and sends it to a detector which has an adjustable pinhole aperture. The emitted light from the spot passes through the pinhole, while the light from outside the spot or off the focal plane is blocked by the pinhole. The advantage of this confocality is a considerable reduction of the depth of focus. This allows us to separate the signal from each layer of a layered sample, thus improving the image resolution.

For μPL maps, we can use two modes of scanning over the sample surface, XYZ motorized and XYZ scanable. In the XYZ motorized mode, the stage moves point by point with respect to the laser beam. In the second mode, the stage is fixed and the laser beam moves on the sample by a motorized mirror. We used the first mode for room temperature PL and the second mode for low temperature PL studies, in which the stage is replaced by a cryostat (see Figure 3.5).

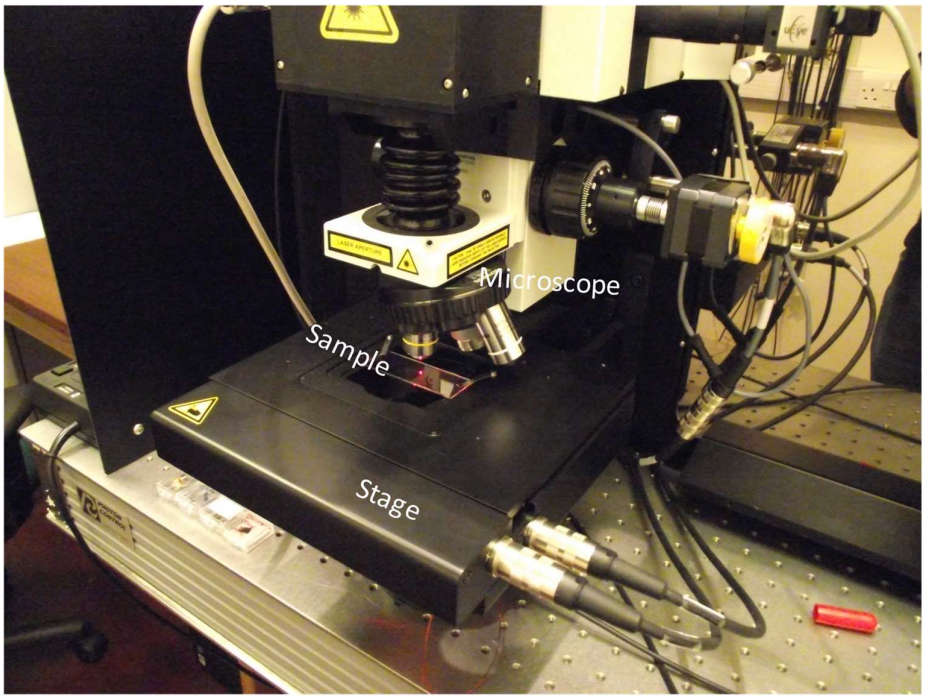

Figure 3.4: Experimental setup for μPL measurements at T = 300 K. Picture shows the microscope, stage, sample and the focused laser beam.

Figure 3.4 shows the experimental setup for PL measurement. The He-Ne laser beam was focused onto the sample by a 100× objective, thus providing a laser spot with diameter $d < 1\mu m$. The size of the spot is determined by the numerical aperture (NA) of the objective

$$NA = n \sin\theta, \tag{3.1}$$

where n is the refractive index of the medium between the lens and the focal plane, and θ is the half angle between the marginal converging rays of the light cone. Using the Rayleigh criterion, the diameter of the spot can be written as

$$d_R = 1.22 \times \frac{\lambda}{NA}. \tag{3.2}$$

For λ = 633 nm and NA = 0.9, we find that d_R = 0.86 μm. This corresponds to the spatial resolution of our confocal microscope. The resolution can be limited by the size of the pinhole. The aperture should be small enough to ensure high spatial resolution and possibly large enough to let sufficient light into the detector.

3.3 Low temperature micro-photoluminescence

For low temperature (T = 5 K) μPL studies, we used the LabRAM HR-UV spectroscope and a Helium flow cryostat (see Figure 3.5). The sample is mounted close to the inner surface of the optical window. The sample holder is a screw mounting arrangement and thermally isolated and tightly fixed on the vacuum housing for low drift. The distance of the sample from the surface can be adjusted from 0 to 3 mm. An external pressure regulator draws a continuous Helium flux from the Helium Dewar to the cryostat through a GFS 600 transfer tube. A temperature meter and heater are connected to the cryostat and permit to measure and control the temperature of the cryostat and of the sample.

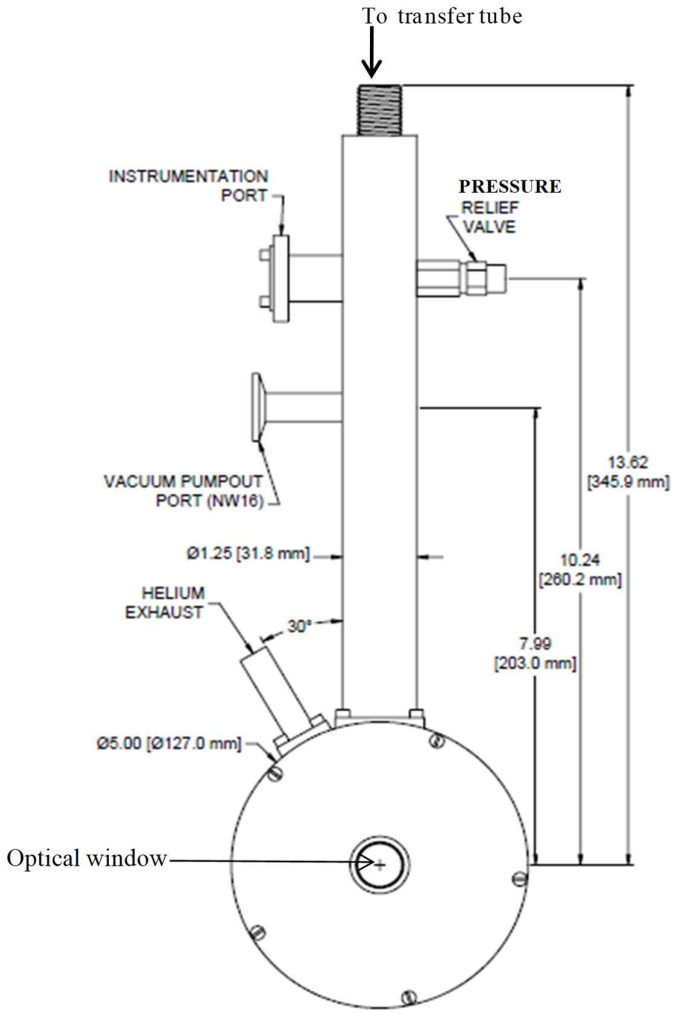

Figure 3.5: Schematic diagram of a Helium flow cryostat (model: Helitran LT-3 OM) for low temperature μPL measurements. Picture reproduced from Ref [47].

3.4 Temperature dependent photoluminescence

The temperature dependent PL measurements (T = 4.2–290 K) were carried out using a TRIAX 550 spectrometer and an Optistat cryostat. The TRIAX 550 spectrograph has an asymmetric optical path for high quality imaging (see Figure 3.6). In our system, the turret has two gratings (600 and 1200 g/mm) and allows the TRIAX to maintain on-axis grating rotation during

the scanning. A high speed drive and precise motorized slits fully automate the adjustments on the TRIAX. The spectrograph is equipped with a Si-CCD and an (InGa)As photodiode array for measurements in the visible or the IR wavelength rage. For our studies of the temperature dependent PL emission, we used a Si-CCD detector and a 600 g/mm grating.

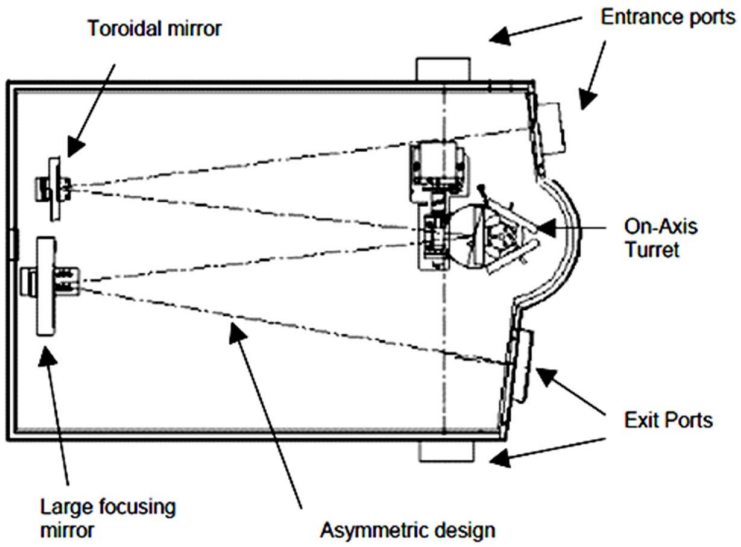

Figure 3.6: Schematic diagram of the TRIAX SERIES 550 spectrograph – top view. Picture reproduced from Ref [48].

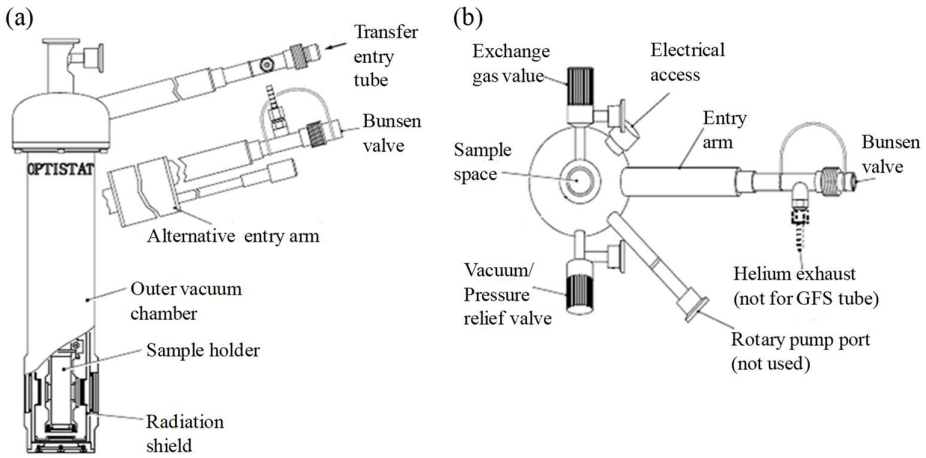

Figure 3.7: Schematic diagram of an Optistat cryostat (a) side view and (b) top view. Picture reproduced from Ref [49].

We used an Optistat cryostat to control the sample temperature, see Figure 3.7. The sample is mounted on a removable sample holder and placed inside the optical window block. The cryostat has four optical windows, and the sample holder can be rotated towards each window. The outer vacuum chamber (OVC) is at room temperature. The sample space and the radiation shields are thermally isolated from the OCV. The Helium Dewar is connected with the cryostat via a GFS 600 transfer tube, which allows us to cool down the sample down to 4.2 K.

The experimental setup for PL measurements is shown in Figure 3.8. The He-Ne laser beam (λ = 633 nm, P ~ 50 W/cm^2) is focused onto the sample by a lens with a focal length of 5 cm, thus providing a laser spot with diameter of ~ 100 µm. The emitted light from the sample is collected by the same lens and then focused by a second lens into the entrance slit of the TRIAX 550 spectrometer. The interferential filter at 633 nm cuts all other wavelengths except the laser line at λ = 633 nm. A temperature meter and heater are connected to the cryostat and permit to measure and control the temperature of the sample space from 4.2 K to 300 K.

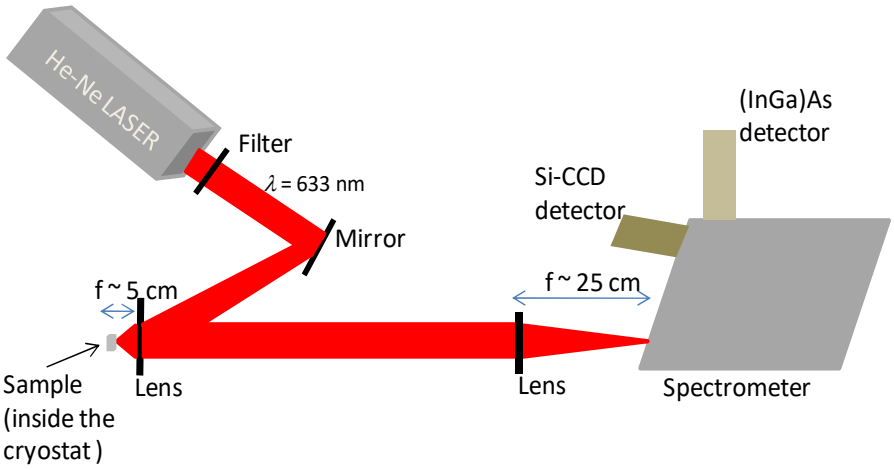

Figure 3.8: Experimental setup for temperature dependent PL studies.

3.5 Laser annealing

For the laser annealing experiments, the laser beam was focused onto the sample thus providing a laser spot with diameter of ~ 1µm. Two different lasers were used, an Ar laser (λ = 515 nm) and a He-Ne laser (λ = 633 nm). We produced annealed spots by using various laser powers (3–120 mW) and exposure times (t_a up to 3 minutes). Figure 3.9 shows the experimental setup for the annealing with the Ar-laser. Here we used a 100× objective and a beam splitter was used to reflect the beam on a screen thus facilitating the visualization of the focussing conditions. We also used a µPL system equipped with a confocal microscope for in-situ He-Ne laser annealing and µPL measurements (see Figure 3.4).

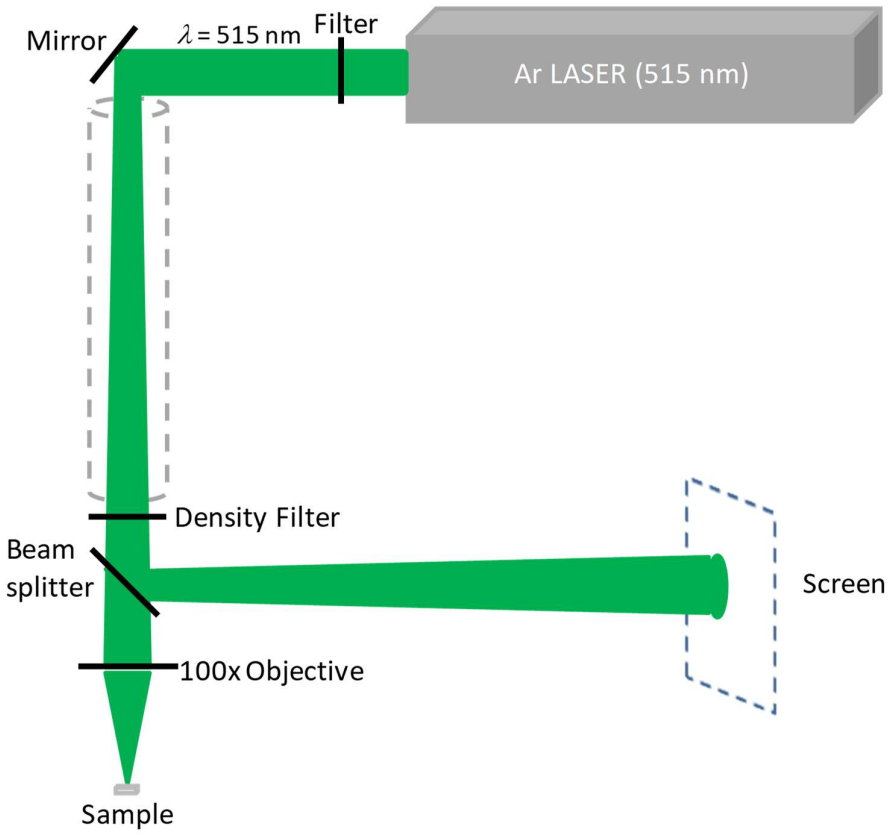

Figure 3.9: Experimental setup for laser annealing with an Ar laser.

3.6 Scanning Electron Microscopy (SEM)

We used an FEI Quanta 200 3D FIB-SEM to probe the hydrogen distribution profile across the laser annealed region. The schematic diagram of the SEM is shown in Figure 3.10. The tungsten filament is heated by an applied voltage thus causing thermionic electron emission. The emitted electron beam is accelerated towards the anode, narrowed by a condenser lens, and focused as a very fine point on the sample by the objective lens. The focused electron beam induces emission of secondary electrons from the sample, which are collected by the electron detector for imaging and analysis. Also, photons emitted by the interaction of the focused electron beam with the sample are detected by the energy dispersive x-ray detector.

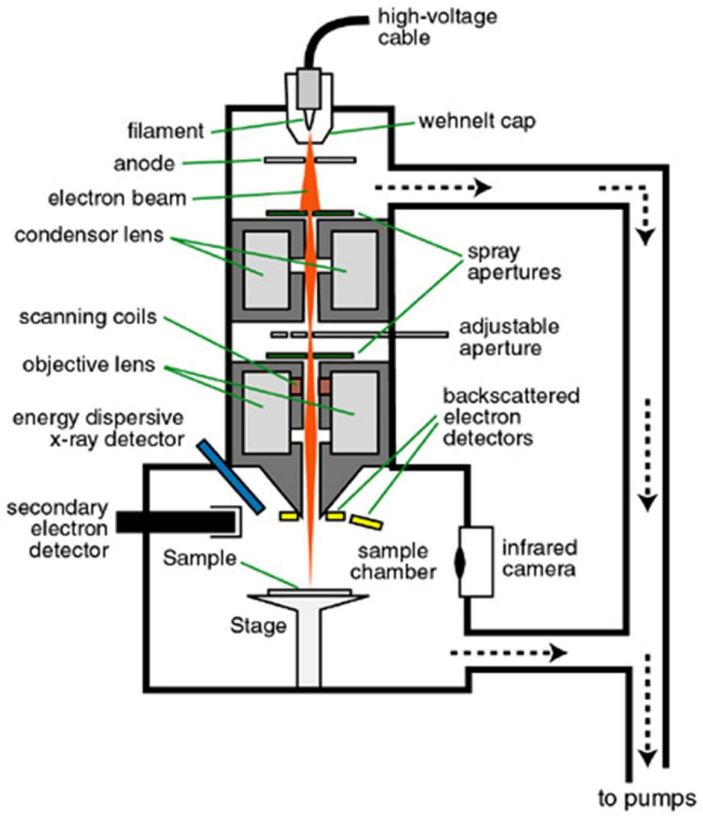

Figure 3.10: Schematic diagram of a Scanning Electron Microscopy. Picture reproduced from Ref [50].

Our SEM system has a spatial resolution of 3.5 nm and 15 nm for an accelerating voltage V = 30 kV and 2 kV, respectively. The spatial resolution also depends on the electron spot size, which can be controlled by the condenser lens, objective lens, position of the filament in the cathode, bias voltage and accelerating voltage. The sample topography at several points is imaged by moving the electron beam with respect to the sample. The sample can be moved with respect to the detector along the x-axis (side by side) and along the y-axis (forward and backward). It can also be tilted and rotated in the plane.

3.7 Atomic Force Microscopy (AFM)

We used a MFP-3D AFM system to probe the surface topographical map of our samples. The AFM has a sub-angstrom resolution in the Z direction (depth) and nanometer resolution in the XY plane. The AFM consists of a low spring constant cantilever with a sharp tip, an IR-laser and a deflection sensor, which is a four-quadrant-photodiode. A schematic diagram of an AFM is shown in Figure 3.11. The sharp tip of the cantilever is very close to the sample surface and during the scanning it reacts in response to the short range repulsive force (~ 10 nN) between the tip and the sample surface. A focused laser beam on the backside of the cantilever is reflected onto a split photodiode, which measures the deflection or oscillation amplitude. Detected changes in the cantilever deflection or oscillation are corrected to a constant value by triggering the cantilever in the Z direction through a feedback controlled piezo. The feedback voltage correlates to a voltage-distance calibration factor, thus determining the height at a given XY coordinate. The AFM image displays the

surface in all three dimensions without the limit of optical diffraction present in the optical microscopes.

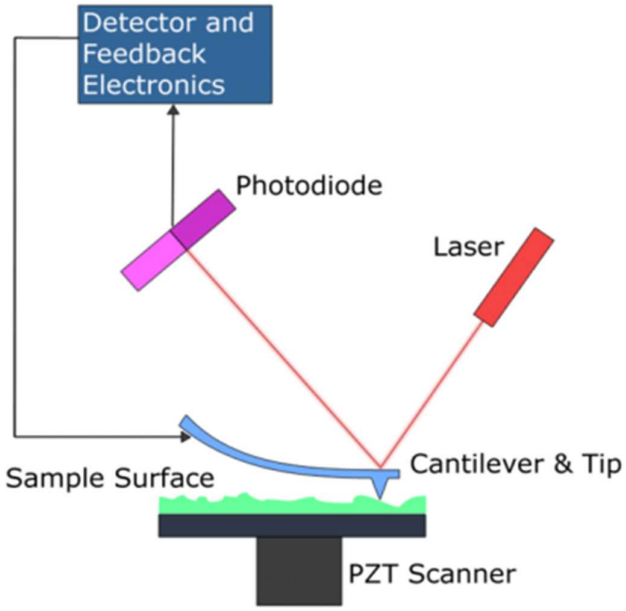

Figure 3.11: Schematic diagram of an Atomic Force Microscopy. Picture reproduced from Ref [51].

Chapter 4

Laser and Thermal Annealing of Ga(AsN)

This chapter describes how a focussed laser beam can be used to control the electronic activity of N- and H-atoms in a Ga(AsN)/GaAs quantum well (QW). Our laser writing technique and micro-photoluminescence (μPL) studies provide real-time in-situ characterisation and control of the N-H complex dissociation and of the band gap energy of Ga(AsN). Also, we use a conventional thermal annealing technique to probe the thermal stability of the laser annealed spots.

4.1 Photoluminescence studies

The PL studies presented in this section were done using an optical confocal microscope equipped with a nanofocusing system and a spectrometer with a 150g/mm grating equipped with a liquid-nitrogen cooled (InGa)As array photodetector. The laser beam (λ = 633 nm) was focused to a diameter $d <$ 1μm using a 100× objective and the μPL spectra were measured at several points by moving the sample with respect to the laser beam.

The incorporation of hydrogen in the Ga(AsN) QW leads to the formation of several complexes including the in-line dihydrogen-nitrogen complex (H_2^*-N), H-N-H complexes with C_{2v} asymmetric or C_{1h} symmetry, and higher order clusters. Complexes with C_{2v} asymmetric or C_{1h} symmetry are the most abundant species [5-7]. They act to neutralize the electronic activity

of nitrogen and its effect on the band gap energy of GaAs, thus causing a blue shift of the QW PL emission [5-7]. This effect is shown in Figure 4.1 for our three hydrogenated samples (H1: $4x10^{16}$ H ions/cm^2, H2: $6x10^{16}$ H ions/cm^2 and H3: $8x10^{16}$ H ions/cm^2), which are compared to the Virgin 'V' (non-hydrogenated) sample. One can notice that the blue shift increases with increasing the hydrogen dose and that in samples H1 and H2 the amount of diffused hydrogen in the Ga(AsN) QW is not sufficient to neutralise all the N-atoms. However, in sample H3 the Ga(AsN) QW peak is fully quenched by H.

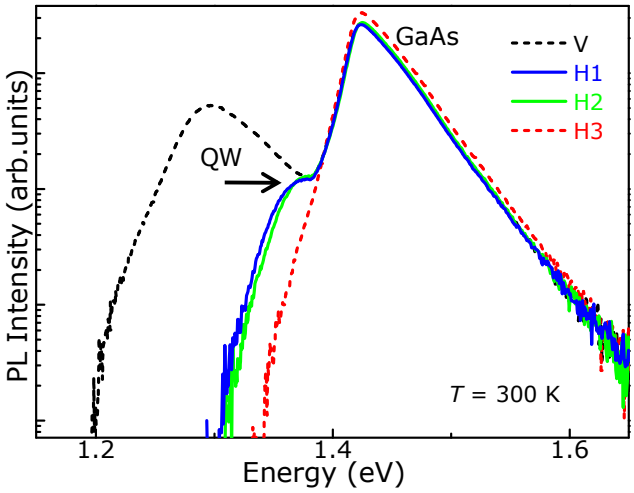

Figure 4.1: μPL spectra of samples V, H1, H2 and H3 at T = 300 K (P = 1.8 mW, λ = 633 nm).

The concentration of electrically active N-atoms in the Ga(AsN) QW of each sample was determined from the peak energy of the QW PL emission, E_{QW}, as shown in Figure 4.2. We model the band gap energy of Ga(AsN) by a two-level band-anticrossing model with an interaction parameter C_{MN} = 2.7 eV and a N-level located at 0.23 eV above the conduction band minimum of GaAs [2]. Also, we solve the Schrödinger equation for a finite square well potential

barrier taking into account the dependence of the electron effective mass on the N-content. As shown in Figure 4.2 the electrically active N content in samples V, H1, H2, and H3 is equal to 0.85%, 0.32%, 0.29% and 0%, respectively. The high resolution x-ray diffraction (HRXRD) measurements indicate that the nominal concentration of N content in the V-sample is equal to 0.9%.

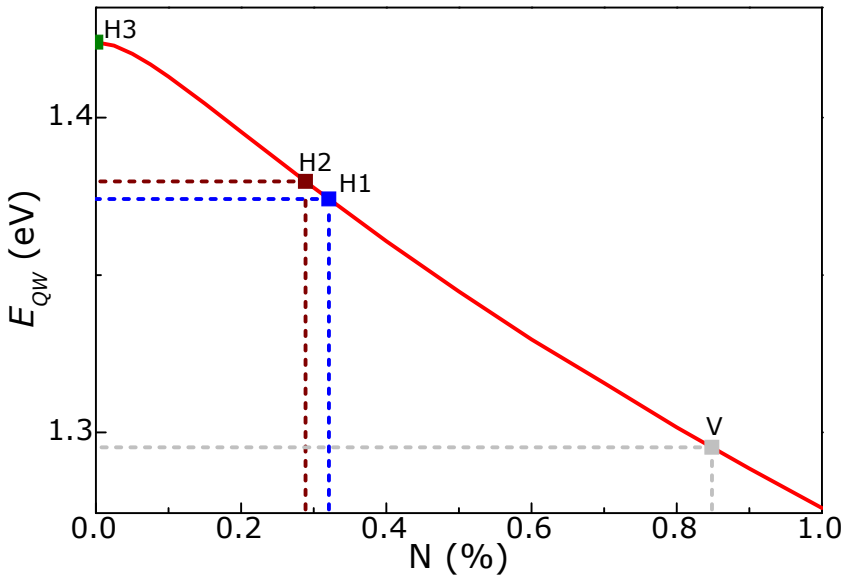

Figure 4.2: Dependence of the peak energy of the QW PL emission (E_{QW}) on N-content as derived from the QW square potential model.

4.2 Laser annealing: preliminary studies

In this section we show how the neutralization of the electronic activity of N by H can be reversed locally using a focussed laser beam, which acts to dissociate the N-H complexes. For the laser annealing experiments, we used a focused laser beam (d~1μm) of wavelength λ = 515 nm, power P_a in the range 10-120 mW, and exposure time t_a = 15 s. A series of light emitting regions were produced at various laser powers at room temperature (T = 300 K). The

μPL intensity maps were measured at low power (P = 1.8 mW) using an He-Ne laser and by integrating the local PL intensity in the spectral range of the QW emission (~1.3 eV), as shown in Figure 4.3 for sample H2. Here one can note that laser powers P_a > 40 mW produce larger spots. Some of these reveal a darker area in their centre. Note that the spot produced with P_a = 10 mW cannot be revealed in this map due to the higher intensity emission from the spots created at higher P_a.

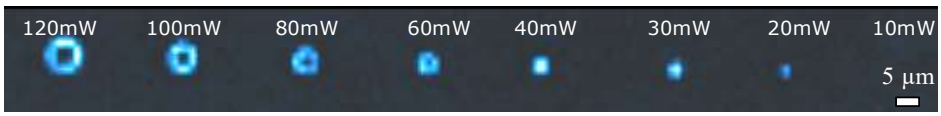

Figure 4.3: Series of spots created by an Ar laser on the H2 sample. The μPL map was obtained by plotting the PL intensity integrated around the energy range of the QW emission (T = 300 K).

Figure 4.4 shows the μPL spectra of all hydrogenated samples measured at low power (P = 1.8 mW) using an He-Ne laser after sample exposure to a focussed laser beam (d~1μm) of wavelength λ = 515 nm and power P_a = 20 and 30 mW for a time t_a = 15s. It can be seen that the effect of the laser exposure is to restore the QW emission observed in the Virgin 'V'-sample. Note that the PL intensity tends to decrease for laser exposures at large powers, i.e. $P_a \geq 40$ mW. These powers lead to a significant heating and a damage of the sample surface [52] due to As-desorption at high temperatures (> 600 C°) [53]. This effect manifests through the appearance of a dark area in the centre of the spots, see Figure 4.3.

The QW PL intensity distribution inside the spots with $P_a \leq 30$ mW has an approximately Gaussian form with a full width at half maximum that corresponds closely to the size of the laser spot diameter (~ 1 μm).

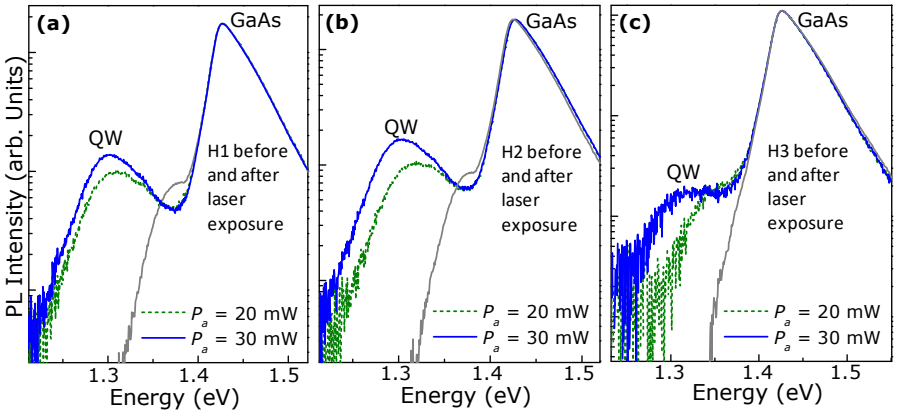

Figure 4.4: μPL spectra of (a) sample H1 (b) H2 and (c) H3 at T = 300 K before and after exposure to a focussed laser beam with power P_a = 20 and 30 mW (t_a = 15 s and λ = 515 nm). All spectra are normalized to the PL intensity of the GaAs PL peak.

4.3 Laser annealing and photodissociation of the N-H complex

The laser annealing technique introduced in section 4.2 can be used to produce arrays of light emitting regions or shaped emitting areas with sub-micron precision, see Figure 4.5a. As shown in Figure 4.5b, the photon energy of the light emitting regions can be controlled precisely by the laser exposure conditions. In Figure 4.5b, we plot the dependence of the peak energy, hv, of the QW PL emission for sample H2 as a function of the exposure time t_a at various powers P_a of an He-Ne laser (λ = 633 nm). It can be seen that the QW PL peak energy shifts to lower energies with increasing t_a until it saturates, more quickly at larger powers.

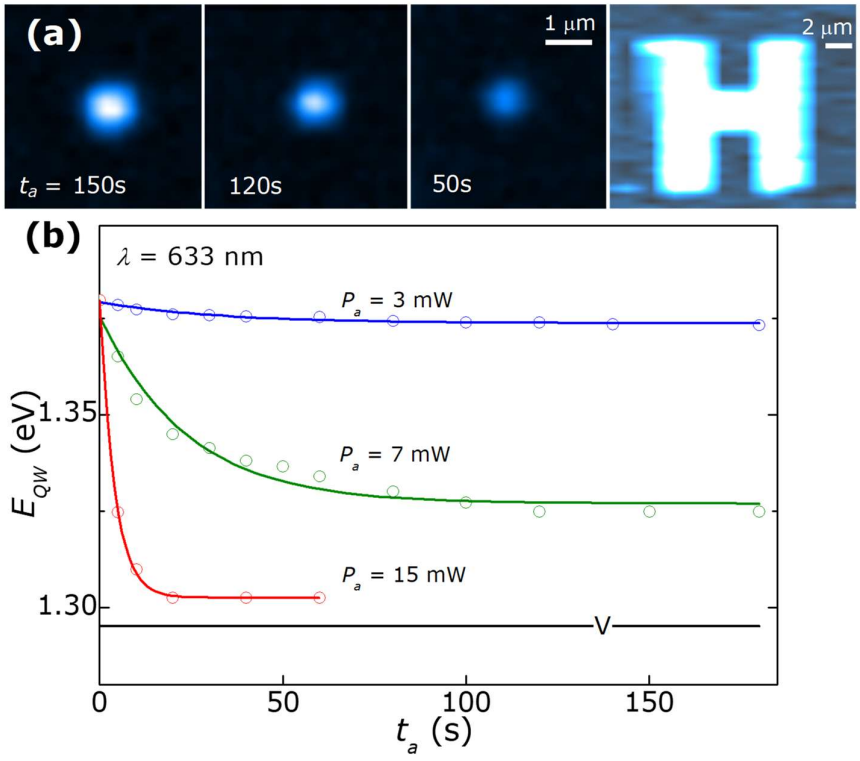

Figure 4.5: (a) Left: μPL intensity maps of sample H2 at T = 300 K following a laser exposure with laser power P_a = 7 mW, exposure times t_a = 150, 120 and 50 s and λ = 633 nm. Right: H-shaped emitting area written by laser (P_a = 15 mW, t_a = 10 s, λ = 633 nm) and mapped using a laser power of 0.1 mW at T = 300 K. (b) Dependence of the peak energy, E_{QW}, of the Ga(AsN) QW PL emission on t_a at T = 300 K (λ = 633 nm). Continuous lines are guides to the eye. The horizontal line corresponds to the value of E_{QW} in the V-sample.

The exposure of the sample to the laser beam can induce a local heating, which we probe by acquiring the μPL spectra during *in-situ* laser exposure experiments with a focussed laser beam (λ = 633 nm). As shown in Figure 4.6a, the high energy tail of the GaAs μPL emission in sample H2 exhibits an exponential tail described by $\exp(-h\nu/k_B T_e)$, where T_e is the effective temperature of the photogenerated carriers. As shown in Figure 4.6b, the value of T_e increases with increasing P_a and/or exposure time t_a. In particular, T_e

increases very quickly during the first few seconds (t_a < 5 s) and increases slowly for t_a > 5 s.

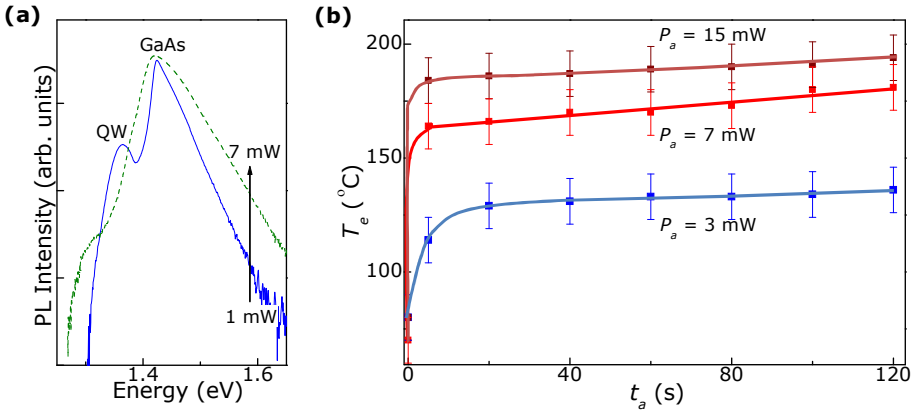

Figure 4.6: (a) PL spectrum of sample H2 measured at various laser powers at T = 300 K (λ = 633 nm). (b) Dependence of the carrier (T_e) temperature on the laser power P_a and exposure time t_a. The solid lines are guides to the eye.

The increase in carrier temperature T_e with increasing laser power P_a is accompanied by an increase of the lattice temperature T_L, which we estimate by modelling the thermal shift of the QW PL peak by the Varshni's law [28], i.e.

$$\Delta E = - \frac{\alpha T^2}{T+\beta} \qquad (4.1)$$

where α = 5.5 x 10^{-4} eV/K and β = 255 K [25]. Figure 4.7a illustrates the PL spectra during and after the laser exposure and the shift of the QW PL peak.

As shown in Figure 4.7b the carrier and lattice temperatures reach values of up to $T_L \sim T_e \sim$ 190 °C at $P_a \sim$ 15 mW and λ = 633 nm. The measured increase of the lattice temperature is in qualitative agreement with that calculated numerically (see Eq. 4.2) [54] by using the temperature dependent thermal conductivity and absorption coefficient of GaAs at λ = 633 nm [55].

According to the model of Ref. 54, the lattice temperature at the centre of the laser spot is given by

$$T_L = \frac{P}{2\pi K(T)} N(\alpha(T,\lambda), d), \tag{4.2}$$

where P is the laser power, $K(T)$ is the thermal conductivity, $N(\alpha(T,\lambda),d)$ is the geometrical coefficient. This depends on the absorption coefficient, α, and the laser spot diameter, d.

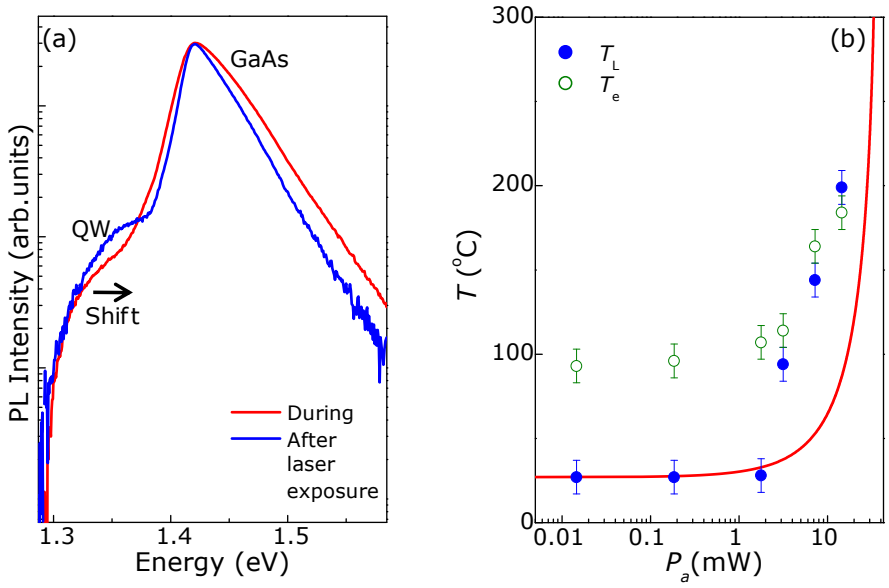

Figure 4.7: (a) μPL spectrum of sample H2 measured during and after exposure to an He-Ne laser (P_a = 7 mW, t_a = 120 s). (b) Dependence of the carrier (T_e) and lattice temperature (T_L) on the laser power (t_a = 120 s, λ = 633 nm). The continuous solid line is the calculated dependence of T_L on the laser power P_a at λ = 633 nm.

Our analysis shows that the laser powers required to trigger the neutralization of the effect of hydrogen on the PL emission energy of the Ga(AsN) QW corresponds to temperatures $T_L \sim T_e \sim 100$ °C ($P_a \sim 3$ mW), which are significantly lower than those (250-300°C) reported before using conventional thermal annealing methods [10]. We note that powers less than

2 mW do not introduce any permanent change in the electronic properties of the hydrogenated QW. On the other hand, laser annealing at powers ≥ 40 mW leads to an abrupt increase of the lattice temperature. This thermal runaway effect is caused by the low thermal conductivity of GaAs at high temperatures.

We evaluate the activation energy for the dissociation of the N-H complexes from the temperature dependence of the increase, ΔN, in the concentration of electrically active N-atoms in the Ga(AsN) QW following the laser exposure. An increase in the value of ΔN is correlated to a corresponding decrease, ΔH, in the concentration of N-H complexes in the QW. We estimate ΔN from our model of the QW emission energy (E_{QW}) and the measured value of E_{QW}.

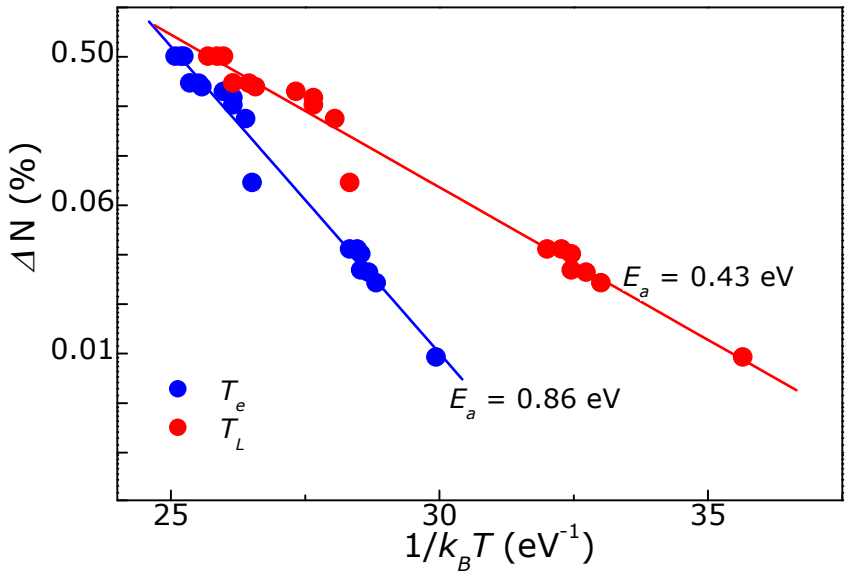

Figure 4.8: Dependence of ΔN on $1/k_BT_L$ and $1/k_BT_e$. The continuous lines are fit to the data by the exponential curve $\exp(-E_a/k_BT)$, where E_a is the activation energy.

The values of ΔN determined under different laser exposure conditions and their dependence on the lattice and carrier temperatures are plotted in

Figure 4.8. The thermally activated behaviour of ΔN, i.e. $\Delta N \sim \exp(-E_a/k_BT)$, is characterized by an activation energy E_a equal to 0.43 eV and 0.86 eV, for T equal to T_L and T_e, respectively. These energies and the corresponding temperatures are significantly smaller than those obtained for the thermal dissociation of N-H related complexes involving one (E_a = 1.77 eV) or two H-atoms (E_a = 1.89 eV) using HRXRD measurements of the lattice parameter during *in-situ* annealing studies at T = 250-300°C [10]. Thus we conclude that our laser writing technique is photon-assisted. Various processes can be envisaged: the photogenerated electron-hole pairs recombine and release their energy to the complex; also, they can modify its charge state, thus reducing the activation energy for the complex dissociation [56]. Similar processes are frequently observed in photochemistry and can be responsible for the light enhanced H motion in amorphous Si [56] and the photo-induced reactivation of neutralized donors in Si-doped GaAs [57].

4.4 Thermal annealing

To assess the thermal stability of the nanoscale light emitting spots created by laser, we used a high temperature furnace and annealed our samples at temperatures ranging from T_a = 25°C to 450 °C for an annealing time t_a = 1 hr. Following the thermal annealing, we allowed our samples to cool down to room temperature and mapped the μPL intensity at low power (P = 1.8 mW, λ = 633 nm) by integrating the local PL intensity in the QW spectral range (~ 1.3 eV), as shown in Figure 4.9 for sample H1.

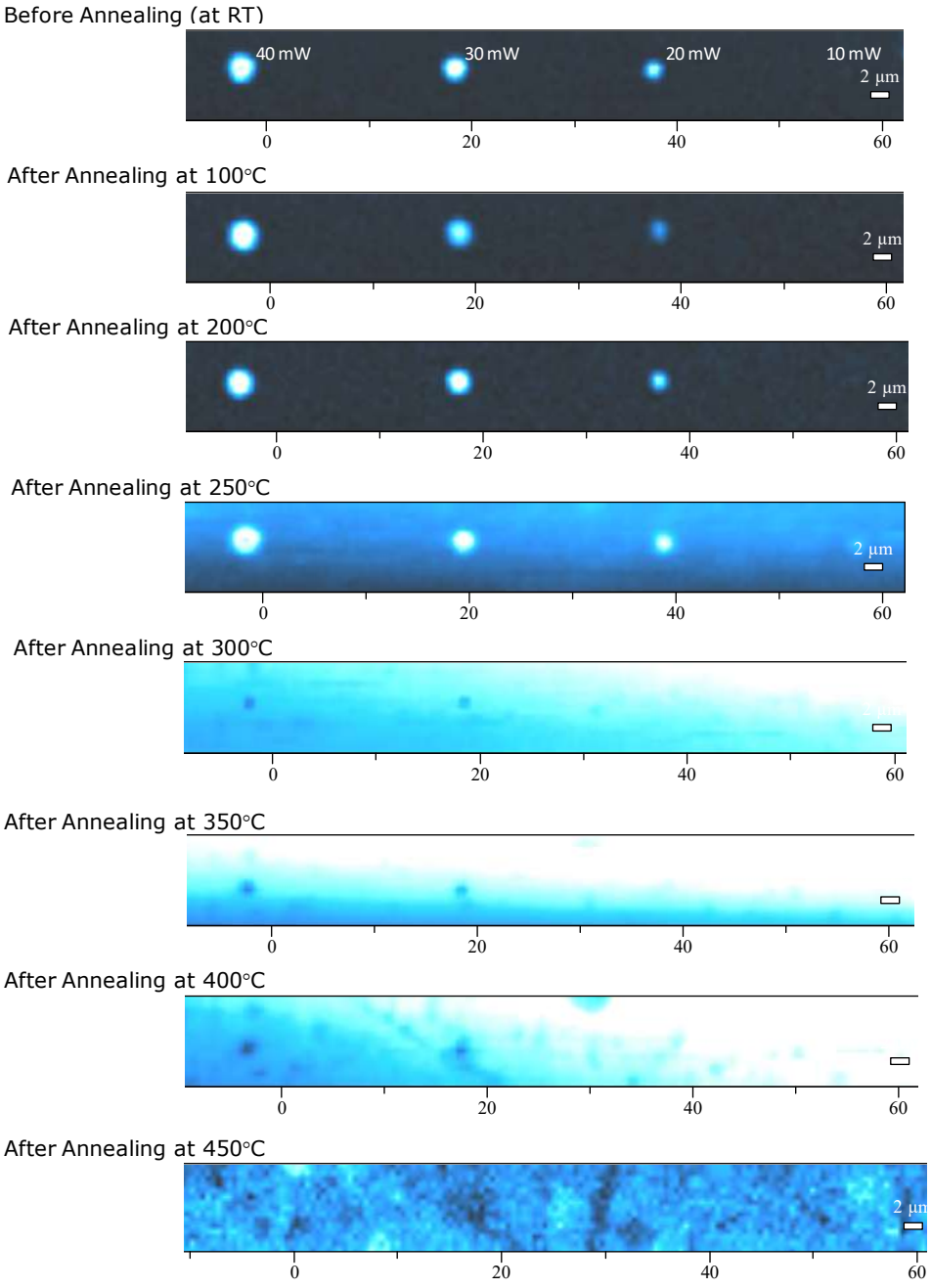

Figure 4.9: µPL intensity maps of sample H1 following a thermal annealing at various temperatures.

For annealing temperature T_a up to 200 °C, the laser annealed spots can be clearly resolved and are not influenced by the annealing. The QW PL intensity inside each spot has an approximately Gaussian form with a full width

at half maximum that does not depend on the annealing temperature. In contrast, for T_a > 200 ˚C we observe a larger contribution of PL intensity from the regions surrounding each spot. At the highest T_a the spots cannot be clearly resolved (T_a ≥ 300 ˚C) and a drop in PL from all regions is observed at T_a = 450 ˚C.

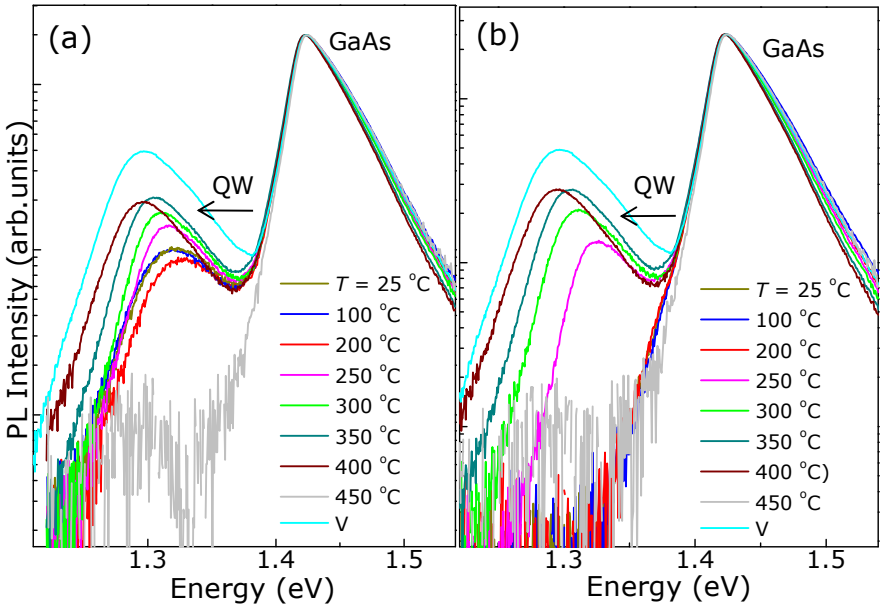

Figure 4.10: µPL spectra at T = 300 K inside (a) and outside (b) a laser annealed spot (P_a = 20 mW, λ = 515 nm) following the annealing in a oven at a temperature T_a.

Figure 4.10a shows the typical µPL spectra of the laser annealed spots and their dependence on the annealing temperature T_a. It can be seen that an increase of T_a from T = 25 ˚C to 200 ˚C tends to blue shift the QW emission. This suggests that the annealing facilitates the formation of a larger number of N-H complexes due to diffusion of H from interstitial positions inside or outside the spot. This blue shift is followed by a monotonic red shift of the QW emission with increasing T_a > 200 ˚C, thus indicating a thermally induced

dissociation of the N-H complex. The QW PL emission quenches at T_a ~ 450 °C. This is likely to be caused by the damage of the surface, which is very close (~ 30 nm) to the QW layer. The dissociation of the N-H at high T_a is confirmed by the analysis of the PL spectra acquired outside the spots. It can be seen in Figure 4.10b that increasing T_a recovers the QW emission as observed in the control (non-hydrogenated) V-sample.

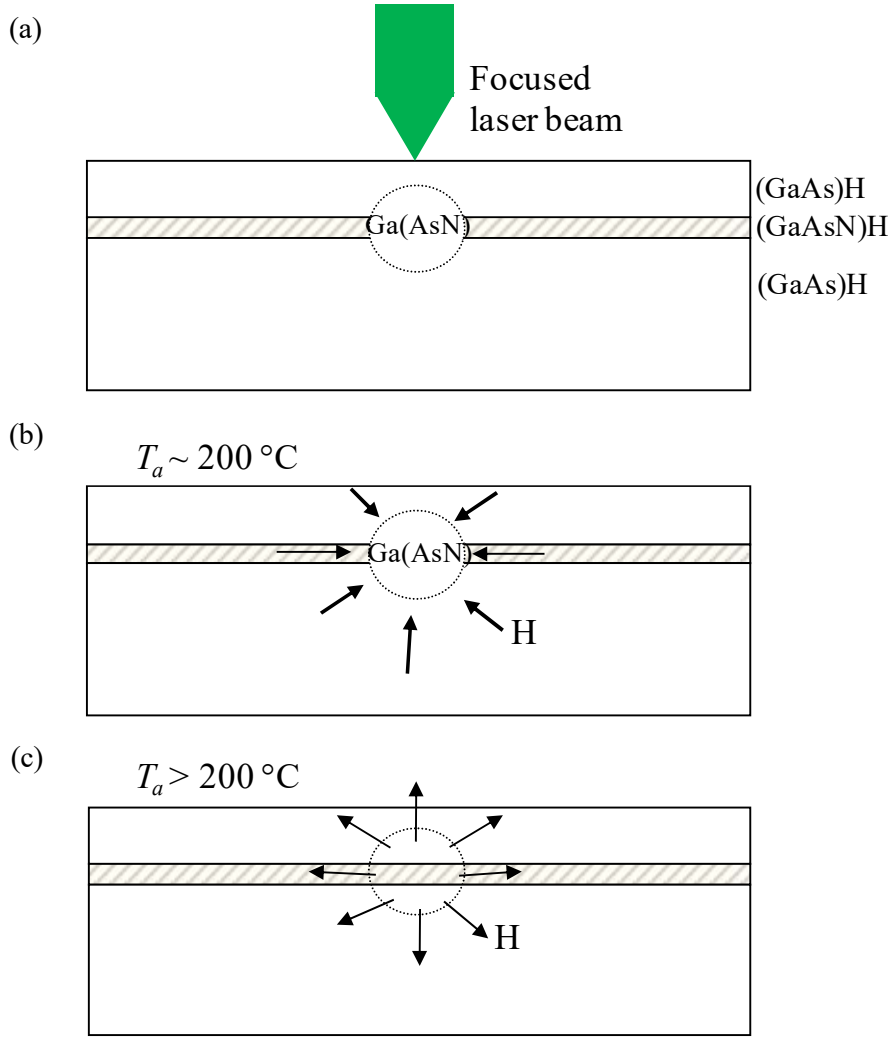

Figure 4.11: Simple model for N-H complex dissociation: laser annealing (a) and thermal annealing at T_a ~ 200 °C (b) and T_a > 200 °C (c).

We illustrate in Figure 4.11 the mechanisms leading to the dissociation/formation of the N-H complex. Laser annealing ($P_a \geq 3$ mW) dissociates the N-H complex in the Ga(AsN) QW. The H-atoms move to nearest interstitial positions without forming bonds with the N, thus the band gap energy of Ga(AsN) can be restored. Thermal annealing at low T_a (< 200 °C) can facilitate the diffusion of H from interstitial positions inside or outside the spot to reform the N-H complex. At T_a > 200 °C, the N-H complex tends to thermally dissociates and H diffuse out of the Ga(AsN) QW.

We estimate the activation energy for N-H complex dissociation by thermal annealing from the temperature dependence of the increase, ΔN, in the concentration of electrically active N-atoms in the Ga(AsN) QW following the annealing. This increase ΔN is equal to the decrease, ΔH, in the concentration of N-H complexes in the QW. We estimate ΔN from the energy position of the QW emission and the band anticrossing model (Figure 4.2). The values of ΔH and their dependence on temperature are plotted in Figure 4.12. At high T_a (> 300 °C), the thermally activated behaviour of ΔH, i.e. $\Delta H \sim \exp(E_a/k_B T)$, is characterized by an activation energy $E_a \approx 1.6$ eV. More data are required to obtain accurate estimates of E_a. However, we note that this energy and the activation temperature $T_a \sim 200$ °C are comparable to those obtained for the dissociation of the H-N-H complex (E_a = 1.77eV and 1.89 eV) using HRXRD measurements of the lattice parameter during *in situ* annealing studies at T_a = 250-300 °C [10].

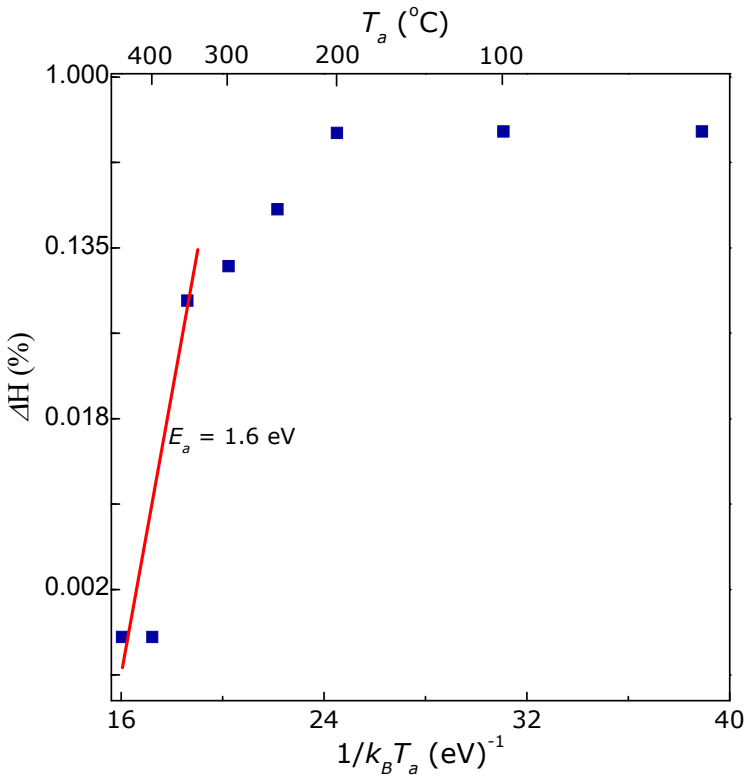

Figure 4.12: Dependence of ΔH on $1/k_BT$. The continuous line is a fit to the data by the exponential curve $\exp(E_a/k_BT)$, where E_a is the activation energy.

Chapter 5

Compositional and Topographical Studies

This chapter describes how the secondary electron (SE) emission in scanning electron microscopy (SEM) can be used to study the surface topography and to map the H-distribution spatial profile across a laser annealed region in an hydrogenated Ga(AsN) QW. The H-distribution profile is well described by a simple model for H-diffusion based on the solution of the Fick's equation. Also, we use atomic force microscopy (AFM) to probe in detail the surface morphology of the laser annealed regions.

5.1 Scanning Electron Microscopy studies

SE imaging by SEM is commonly used to study sample topography with nanometer spatial resolution [58]. In-plane band gap modulations caused by compositional variations can be also detected with higher resolution than in μPL or cathodoluminescence (CL) [59]. Our experimental set-up for SE imaging uses a focused electron beam and a gaseous secondary (Everhart-Thornley) detector. The electron beam was focused to a small spot of diameter $d \sim 185$ nm using an accelerating voltage V = 2 kV. Images of the sample topography were acquired at several points by scanning the electron beam on the sample surface.

First we produced an array of laser annealed spots in sample H2 ($6x10^{16}$ H ions/cm^2). We used a focused laser beam ($d \sim 1\mu m$) of wavelength $\lambda = 515$

nm, powers P_a = 20–120 mW and an exposure time t_a = 15 s. Figure 5.1 shows the image of the annealed spots taken by (a) an optical microscope, (b) the QW µPL and (c-d) SEM. We note that the optical microscope could not resolve the laser annealed spots at powers P_a = 20 and 30 mW. However, µPL and SEM allowed us to resolve all spots and reveal interesting features, as discussed below.

First, for powers $P_a \geq 40$ mW, the SEM and µPL maps reveal the formation of crater-shaped spots. These powers correspond to power densities larger than 10^7 W/cm^2 and lead to a significant heating and damage of the sample surface due to As-desorption [53]. The diameter D of the craters can be determined accurately by SEM, which has a higher spatial resolution (~ 0.1 µm) compared to that in µPL (~1 µm). We find the D increases from ~ 0.1 µm to 3.4 µm with increasing P_a from 40 mW to 120 mW.

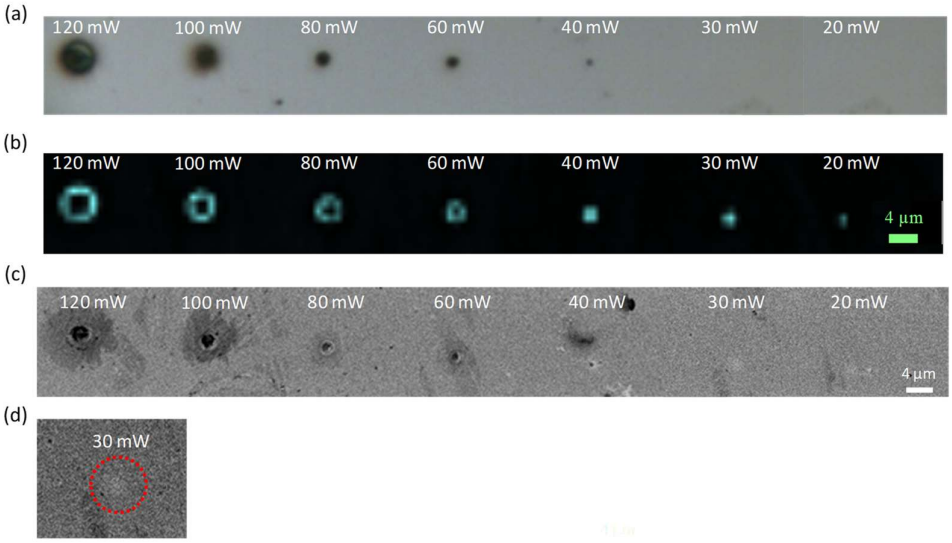

Figure 5.1: Image of the array of laser annealed spots (λ = 515 nm, P_a = 20–120 mW, t_a = 15s) in sample H2 by optical microscopy (a), µPL (b) and SEM (c) & (d).

The SEM images of the annealed regions at $P_a \leq 40$ mW also reveal the existence of brighter areas. These can be resolved more clearly in Figure 5.1d. We explain these regions as follows. The laser annealing dissociates the N-H complexes in the hydrogenated Ga(AsN) QW and facilitates H-diffusion. This causes a SE contrast variation due to the band gap energy and refractive index modulation in the QW plane [59-60]. When the scanning electron beam hits the sample, low energy SEs are generated due to the electron excitation from the valence band to the conduction band [59]. The SEs can reach the surface (depending on the escape depth) and overcome the surface potential barrier if they have enough kinetic energy [59]. The presence of impurities induces a fluctuating potential on the surface [59, 61-62]. The incorporation of H in Ga(AsN) tends to passivate the impurities as well as the electronic activity of N [3-4] and thus acts to change the surface potential fluctuation leading to a change in the escape rate of SEs [59, 61-62]. This can explain the contrast difference between H-free and H-incorporated Ga(AsN) in the SEM images, which is further discussed in section 5.2.

5.2 Probing the H-distribution spatial profile

In this section we discuss how SEM can be used to map the H-distribution profile across the laser annealed regions. We used sample H0 ($2x10^{16}$ H ions/cm^2) and a focused laser beam ($d \sim 1\mu m$, $\lambda = 515$ nm, $P_a = 20$ mW) to draw a line of length $l = 40$ μm in between two laser annealed craters annealed at higher powers ($P_a = 80$ mW). Figure 5.2 shows the SE image (V = 1 kV and I = 110 pA) of the laser annealed line and craters with spatial

resolution of d_R = 0.2 μm. The contrast variation between the laser annealed and the non-annealed regions can be clearly revealed.

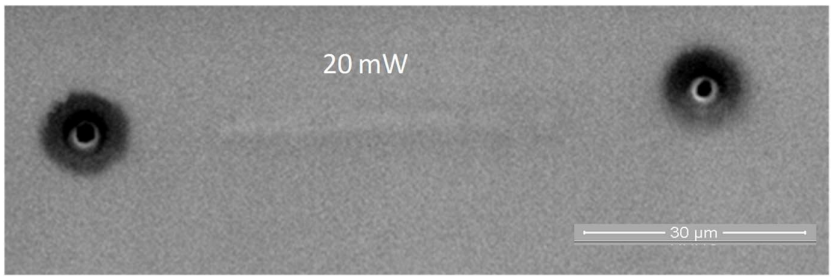

Figure 5.2: Image of a laser annealed line and craters by SEM (V = 1 kV, I = 110 pA).

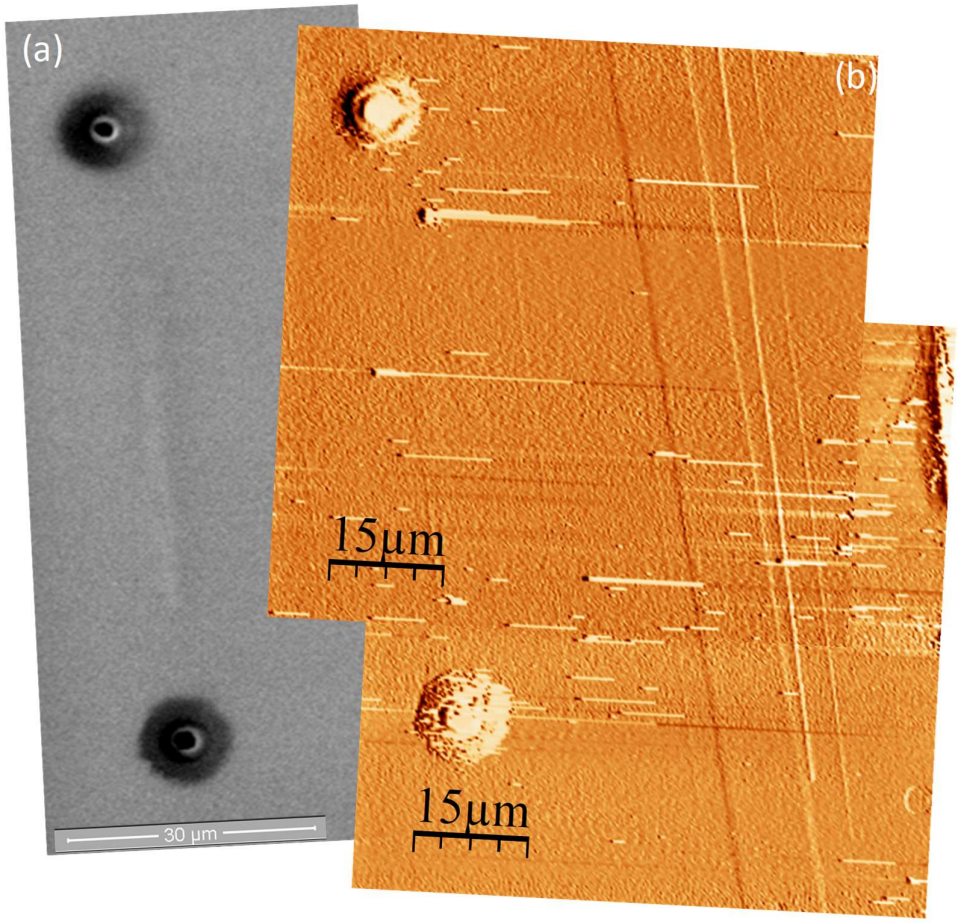

Figure 5.3: Image of a laser annealed line (P_a = 20 mW) by (a) SEM and (b) AFM.

We used atomic force microscopy (AFM) to probe the surface morphology in more detail, see Figure 5.3. To resolve atomic-scale structures, we operated the AFM in the contact mode. In the contact mode, the cantilever tip is scanned over the sample surface in order to keep constant the short range repulsive force (~10 nN) between the surface and the AFM tip [63]. The AFM image reveals that the surface between the craters is not damaged. The white horizontal lines and spots may due to dust particle on the surface. The vertical lines may due instead to the cracks produced by surface polishing.

We probed the hydrogen distribution across the laser annealed line using SEM. The contrast in SE imaging is due to ionized dopants rather than the total number of dopant atoms [64] and depends on material properties (band gap, ionization energy, doping type and content), sample surface effects (contaminants and oxides) and experimental conditions (working distance, detector, accelerating voltage and beam current) [62]. Hydrogen incorporation in semiconductors tends to passivate both deep and shallow crystal defects and dopant atoms [3-4]. In this experiment we assumed that the contrast in the SEM images corresponds to the H-content variation in the Ga(AsN) QW plane.

Figure 5.4a shows the SEM image of a laser annealed line. The corresponding variation of the H-content along the x-direction is shown in Figure 5.4b. Inside the annealed region, the H profile corresponds to an inverted Gaussian with a minimum due to a low H-content. The outside region contains a higher H-content and it decreases along the x-direction far from the centre of the annealed line. This distribution indicates that the laser annealing acts to diffuse the H-atoms outward from the centre of the annealed area. Also

we note that the non-uniform distribution of H-content in the regions far from the annealed line may be due to a non-uniform background SE emission caused by surface contamination [62].

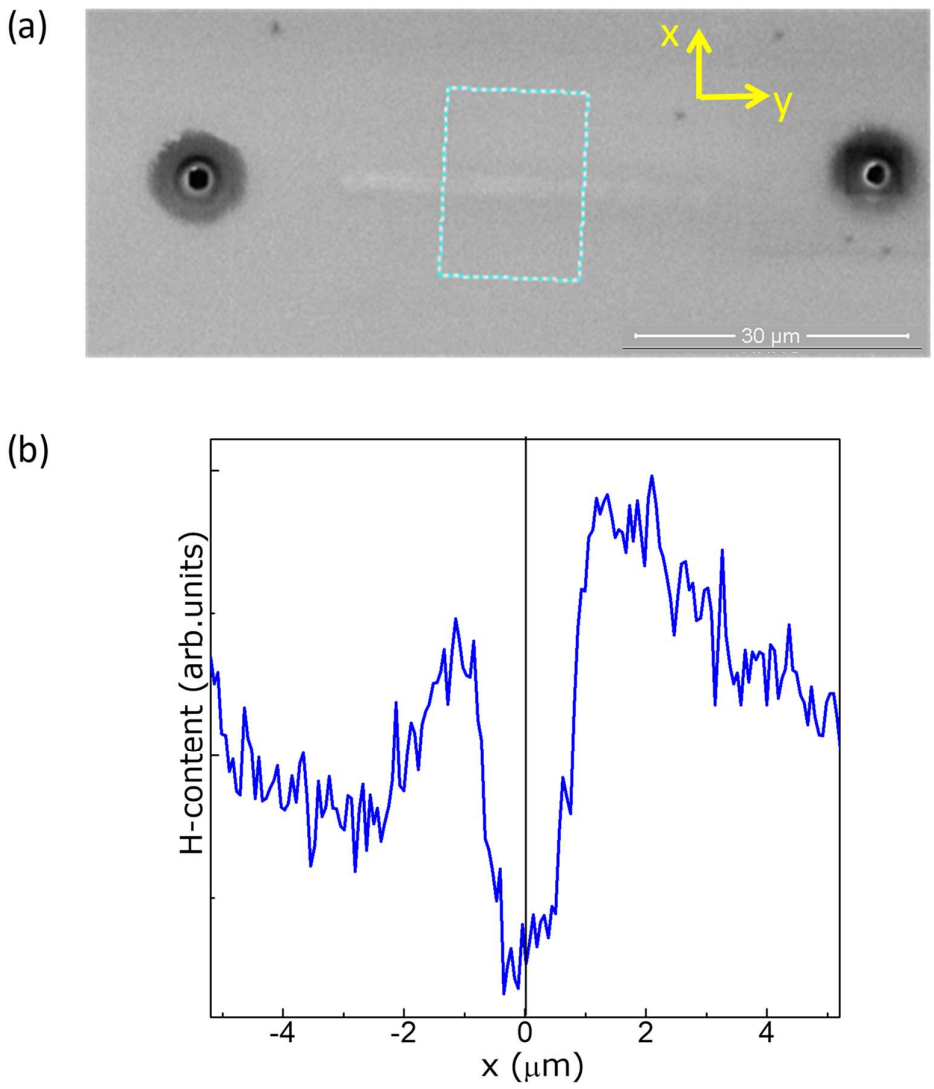

Figure 5.4: (a) SEM image and (b) dependence of H-content on distance x across the laser annealed line shown in part (a). x = 0 corresponds to the position of the line.

5.3 Modelling H-diffusion

In this section we model the H-distribution profile by using the Fick's equation for H-diffusion in one dimension [65]. The concentration of H along x and at time t is given by

$$C(\mathrm{x}, t) = \frac{S}{\sqrt{\pi D t}} \exp\left(-\frac{\mathrm{x}^2}{4Dt}\right), \tag{5.1}$$

where $D(T) = D_0 \exp(-E_d/k_B T)$ is the diffusion coefficient, T is the lattice temperature (≈ 500 K for P_a = 20 mW), t is the annealing time (≈ 1sec), S is the total amount of hydrogen atoms, E_d is the diffusion energy barrier (which we assume to be equal to the energy of the N-H complex dissociation E_a = 0.86 eV), and x = 0 is the centre of the annealed spot.

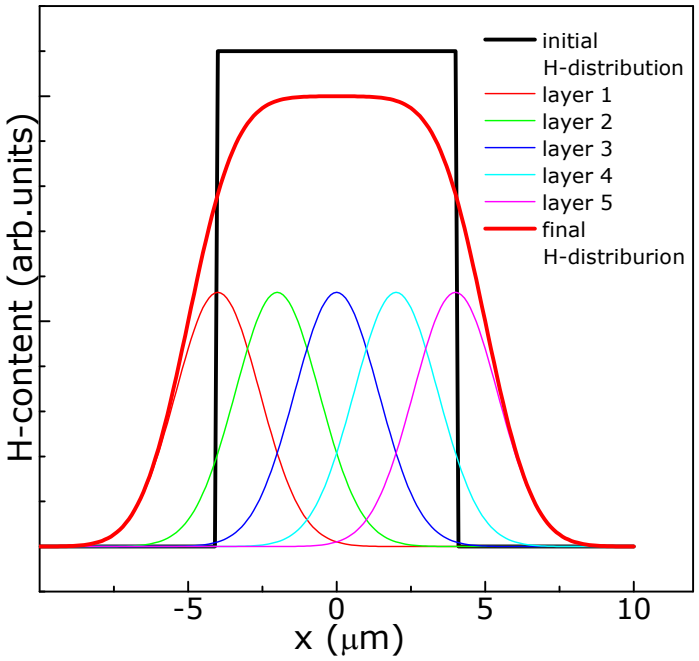

Figure 5.5: Model for H-distribution profile along x based on a numerical algorithm.

The numerical algorithm for the lateral diffusion problem can be demonstrated by a simple example (see Figure 5.5). We assume that the initial

H profile has rectangular shape (black line). We slice this rectangle into a number of independent layers and write the Fick's equation for each layer to obtain a set of Gaussian profiles (thin colour lines in Figure 5.5). Then the final hydrogen distribution is obtained by the summation of these profiles (red line in Figure 5.5). Accuracy of this method increases with increasing number of slices.

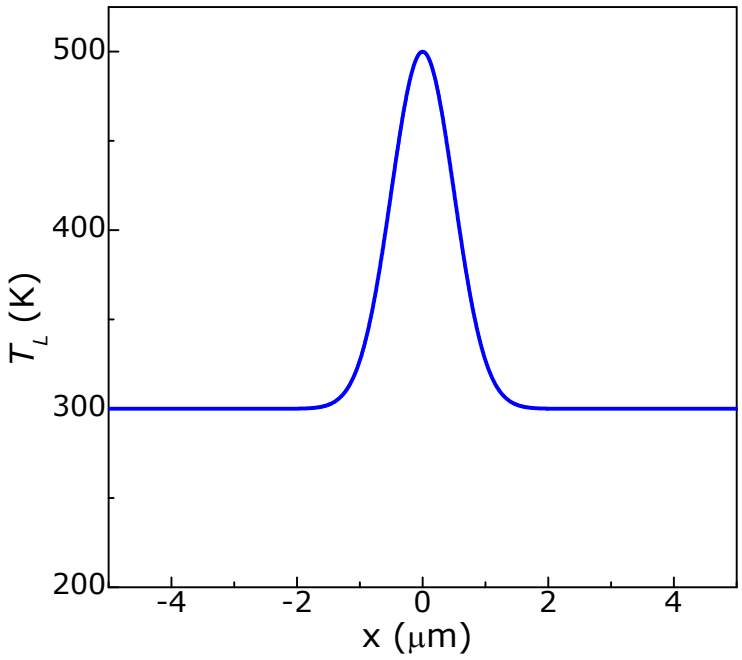

Figure 5.6: Temperature profile for a focused laser beam of maximum power P_a = 20 mW and diameter d = 1 μm according to the model of Ref. 54.

We use this technique to model the H-diffusion. In this case we need to consider the non uniform temperature distribution caused by the focussed laser beam. We assume that the temperature profile is the same as that of the laser intensity Gaussian profile [54]. The temperature profile for a laser spot of diameter d ~ 1μm and maximum power P_a = 20 mW is shown in Figure 5.6.

Hence we use the numerical algorithm and the temperature profile to calculate the H-distribution along x. As shown in Figure 5.7 this model fits well the measured H-distribution profile across a laser annealed line. The H-accumulation layers at a distance ~ 2μm from x = 0 are caused by the slowing down of H atoms that diffuse from the hot centre to the colder regions outside the line [54]. Our model considers the H-diffusion along a given direction and does not include the out-diffusion of H along other spatial directions. This could account for the small discrepancy between the model and our experimental data in Figure 5.7.

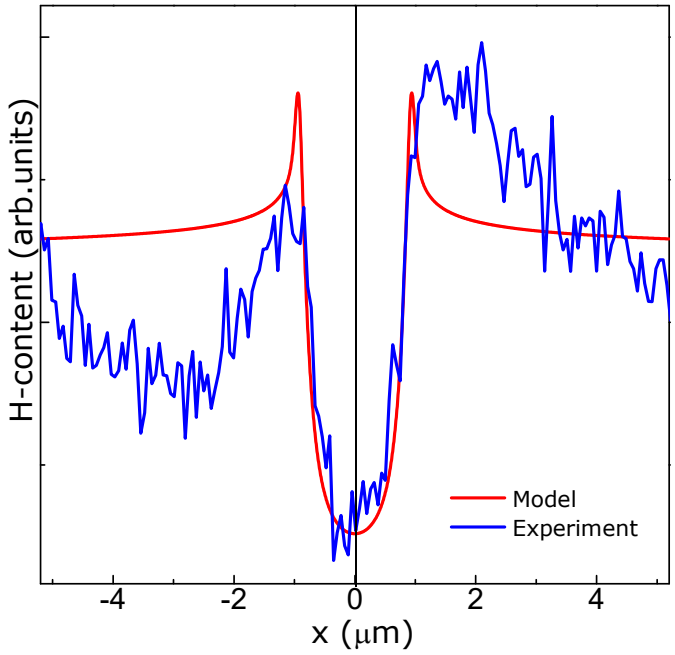

Figure 5.7: Measured and calculated profile of H-distribution across a laser annealed line (P_a = 20 mW).

5.4 Electron writing by SEM

To study the effect of the electron beam on the electronic properties of our samples, we considered focused electron beams with different parameters, i.e. different values of the accelerating voltage (V), the beam current (I), and the working distance (z) (listed in Table 5.1). The SEM image of the annealed lines written by SEM in sample H2 were mapped at V = 2 kV as shown in Figure 5.8a. The lines produced at higher I and larger z are clearly resolved in this figure as darker lines. These lines are wider compared to the lines produced with the same V, but lower I and z. The dark contrast is associated with the effect of the electron beam on the hydrocarbons on the sample surface [66]. The SE emission is extremely sensitive to the surface conditions as these affect the kinetic energy of the SEs that can overcome the surface potential barrier [67]. We used plasma cleaning to remove the hydrocarbons from the sample surface. However, it is extremely difficult to prepare a perfectly clean sample as the hydrocarbons are also present in the vacuum system of the SEM [64, 67].

Table 5.1: Electron writing parameters V, I and z in sample H2.

Line no	Spot size (nm)	t_a (s)	V (kV)	I (nA)	z (μm)
1	185	60	2	0.029	0.05
2	185	60	2	6	11
3	171	60	15	0.036	0.076
4	171	60	15	7.6	15
5	170	60	30	0.097	0.099
6	171	60	30	9.7	20.59

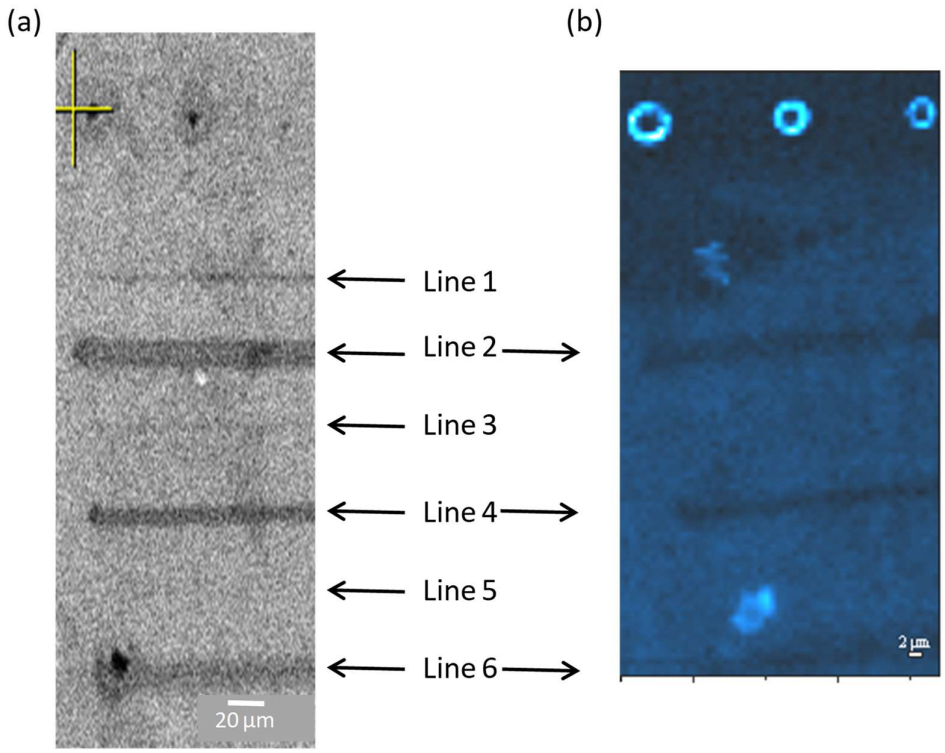

Figure 5.8: Image of electron annealed lines and laser annealed spots by (a) SEM and (b) µPL. The µPL map was obtained by plotting the PL intensity integrated around the energy range of the Ga(AsN) QW emission.

The µPL intensity maps for the electron annealed lines were obtained at low laser power (P = 0.2 mW) by integrating the local PL intensity in the spectral range of the QW emission (~1.3 eV), as shown in Figure 5.8b. These maps can reveal only the lines produced at higher I and larger z. However, brighter emitting regions were not produced by any of these lines thus indicating that the electron beam does not modify the electronic properties of the Ga(AsN) QW. This has confirmed by the PL spectra of Figure 5.9 for the annealed line 2 (V = 2 kV, I = 6 nA), line 4 (V = 15 kV, I = 7.6 nA) and line 6 (V = 30 kV, I = 9.7 nA) and the non-annealed region. Note that the energy of the QW PL emission (~ 1.37 eV) does not change with increasing electron

energy and/or beam current. Only the PL intensity decreases with increasing V and/or I.

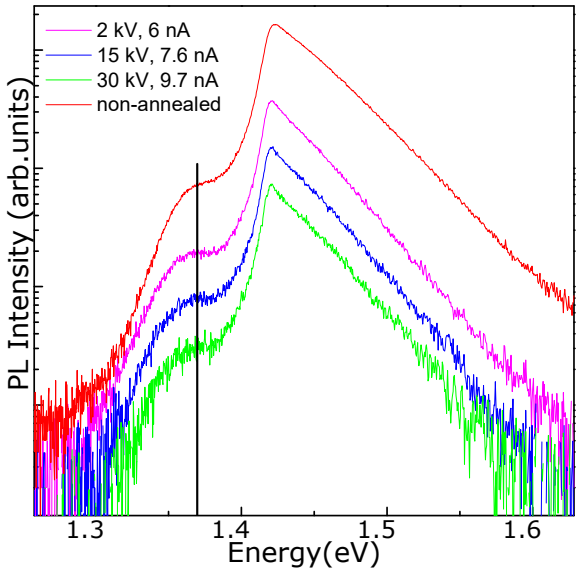

Figure 5.9: μPL spectra of the electron annealed lines in sample H2 at T = 300K (P = 0.2 mW and λ = 633 nm).

The H-incorporation in the Ga(AsN) QW leads to the formation of H-N-H complexes that neutralize the electronic activity of the N-atoms [42-43]. The QW PL energy depends on the amount of electronically active N atoms. Since following the electron writing experiment we do not observe any energy shift in the QW PL emission, we conclude that the electron beam does not dissociate the N-H complexes.

Chapter 6

Low Temperature Photoluminescence Studies

This chapter describes the low temperature photoluminescence (PL) of samples V (non-hydrogenated), H1 ($4x10^{16}$ H ions/cm^2) and H2 ($6x10^{16}$ H ions/cm^2). The PL spectra reveal sharp lines, which we attribute to carrier recombination from N-related states. Also, we study the temperature dependence of the PL emission to investigate the influence of the hydrogen on the optical properties of the Ga(AsN) QW. This study reveals a non-monotonic temperature dependence of the QW peak energy.

6.1 Low temperature micro-photoluminescence

Our experimental arrangement for low temperature μPL measurements comprises a cryostat with an optical window, an optical confocal microscope equipped with a nanofocusing system, and a spectrometer with a 150 g/mm grating equipped with a liquid-nitrogen cooled (InGa)As array photodetector (described in Section 3.2 and 3.3). The temperature of the cryostat is controlled by a pressure regulator during a continuous flux of Helium (He). A temperature meter and heater are connected to the cryostat and permit to measure and control the temperature of the sample. The laser beam (λ = 633 nm) was focused to a diameter $d \sim 1\mu m$ using a 50× objective and the μPL spectra were measured at several points by moving the sample with respect to the laser beam.

Photoluminescence provides a useful tool for the study of impurities, including N-related complexes in Ga(AsN), which manifest in the PL spectra through the appearance of sharp lines, each associated with a specific energy level within the forbidden energy gap [34].

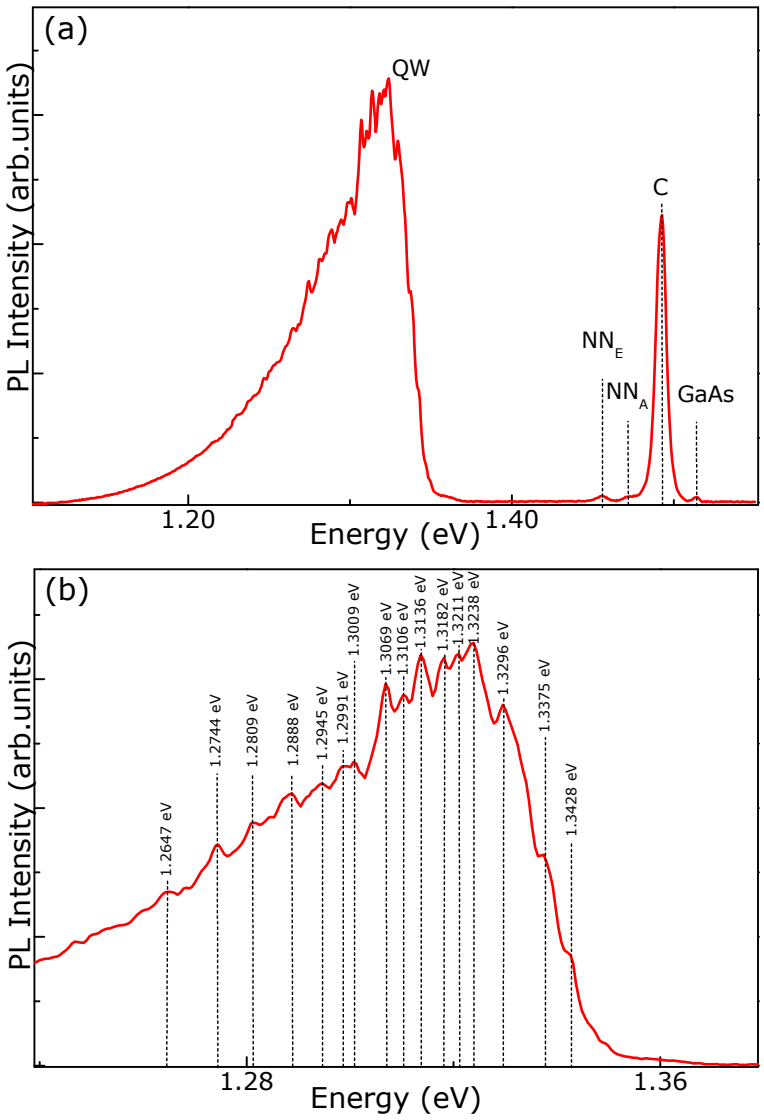

Figure 6.1: (a) μPL spectra of the V-sample at T = 5 K (P = 0.2 μW, λ = 633 nm). Sharp lines in the μPL emission of the QW are shown in part (b).

Figure 6.1a shows the μPL spectrum of the V-sample at T = 5 K. This reveals the GaAs free exciton emission at 1.5144 eV, the Carbon 'C' related emission at 1.4929 eV [68] and two N-related transitions, NN_A at 1.4559 eV and NN_E at 1.4719 eV [34, 68]. The NN_A and NN_E lines are due to the recombination of excitons bound to N-complexes and their energy position is independent on the N concentration [69-70]. The C-acceptor related transition indicates that the sample is p-type due to the inevitable existence of C-atoms in the MBE chamber [70]. Also, we observed that the QW PL emission consists of several sharp lines. These are due to recombination of carriers localized in local minima of the disordered QW potential caused by alloy disorder [26]. In particular, the low energy tail of the QW PL emission can be accounted for by alloy compositional fluctuations [26, 30-32]. These tend to give rise to an exponential density of localized states thus resulting in broad and asymmetric PL line shapes as also reported in the literature [31-32].

We now examine the optical properties of the hydrogenated QW sample. In the PL spectrum of Figure 6.2a, one can identify the PL due to the GaAs free exciton at 1.5144 eV, the Carbon acceptor related transition at 1.4929 eV [68], and the QW band emission made of a number of sharp lines. Note that the QW PL band becomes narrower in the H2 sample compared to that of the V-sample. The sharp lines measured in the V-sample quench and new sharp lines appear in H2 due to the hydrogenation. These data clearly shows that H acts to neutralize the electronic activity of N in the Ga(AsN) QW, thus blue shifting the QW PL emission.

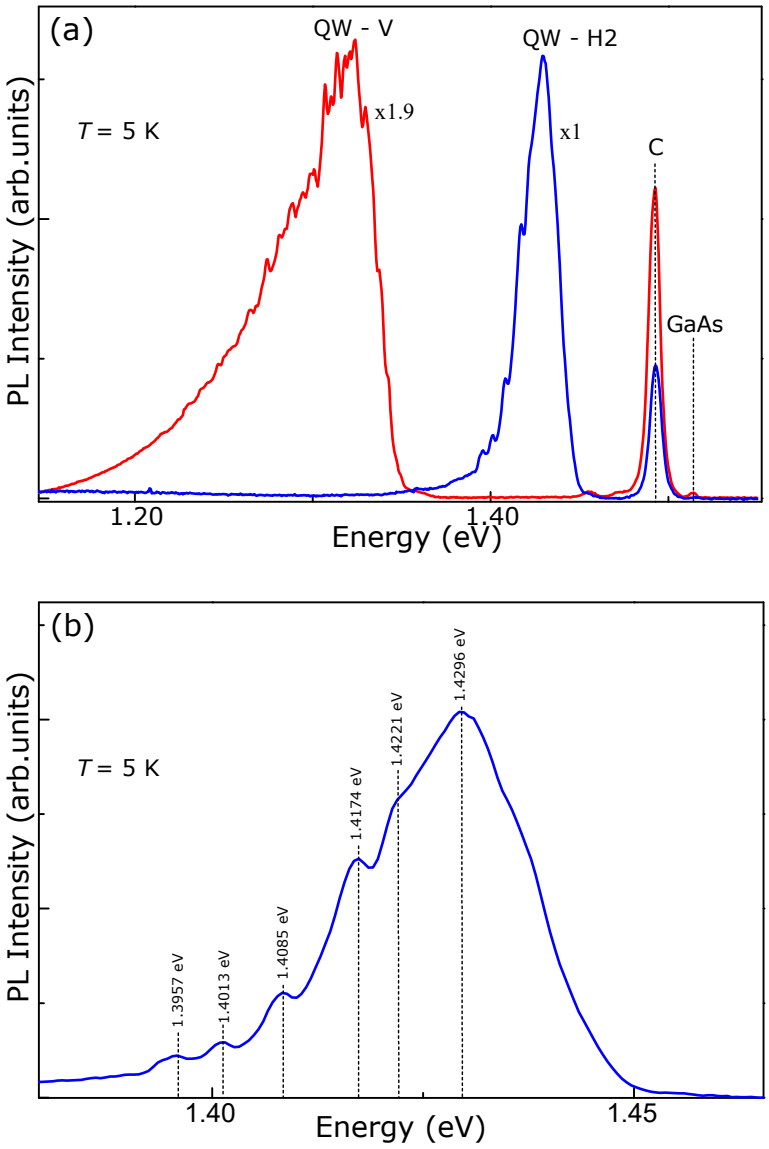

Figure 6.2: (a) μPL spectra of the V and H2 samples at T = 5 K (P = 0.2 μW, λ = 633 nm). Sharp lines in the μPL spectra of the H2 sample are shown in part (b).

6.2 Laser annealing and low temperature micro-photoluminescence

In section 4.2, we discussed our laser annealing technique and how this can reverse the QW blue shift caused by the hydrogen incorporation in a

Ga(AsN) QW. Here, we analyze the PL emission inside and outside the laser annealed spots at low temperature.

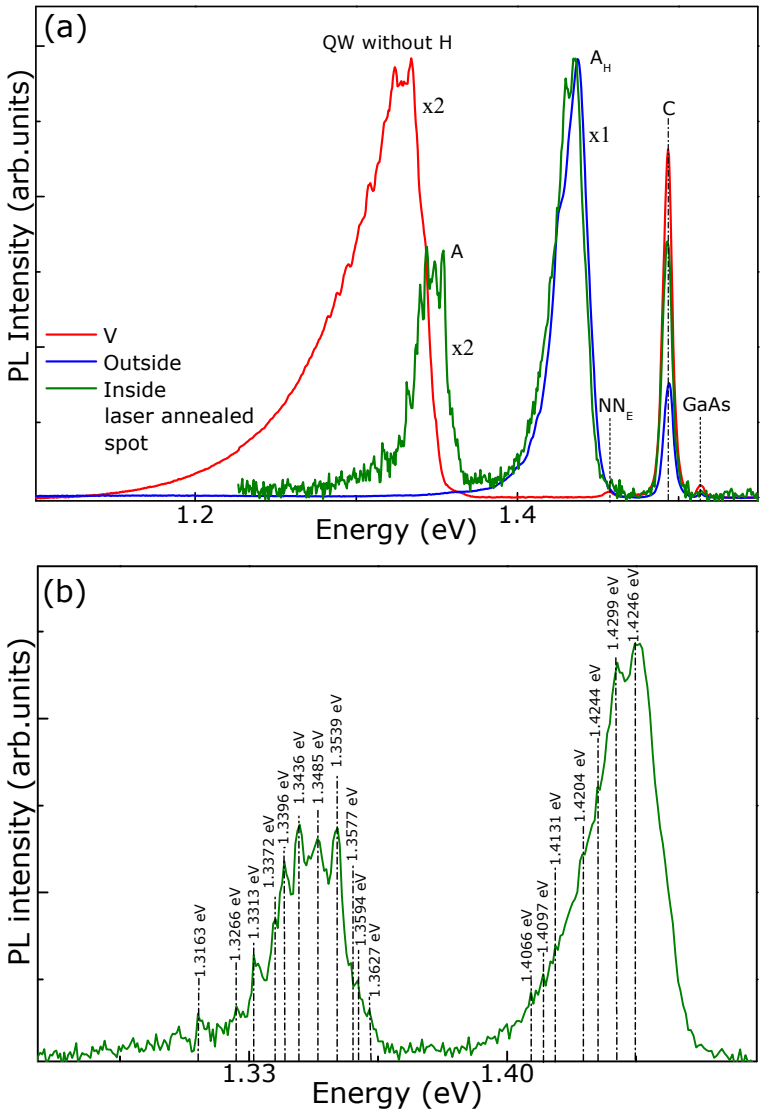

Figure 6.3: μPL spectra of the V-sample and sample H2 inside and outside a laser annealed spot (P_a = 20 mW and λ = 515 nm). Sharp PL lines for the laser annealed spot are shown in part (b).

Figure 6.3a shows the μPL spectra of the H2 sample measured at low power (P = 2 μW) after sample exposure to a laser of power P_a = 20 mW for a time t_a = 15 s. In this Figure we show the μPL spectra measured inside and

outside the laser annealed spot and compare them with the PL spectra of the V-sample. It can be seen that the laser annealing induces the appearance of a PL band at around 1.35 eV (band A), between the PL emission of the QW in the V-sample and that in the hydrogenated sample (band A_H). Band A persists up to room temperature and is associated with carrier recombination from regions of the QW where the laser induces the dissociation of the N-H complex. The persistence of the QW emission at ~ 1.42 eV (band A_H) in the annealed spot indicates the presence of H in some regions of the QW. From this result, we can conclude that the laser annealing tends to dissociates N-H complexes in the QW and that this dissociation is only partial. As shown in Figure 6.3b all PL emissions from the QW consist of sharp lines, thus indicating carrier recombination from localized states.

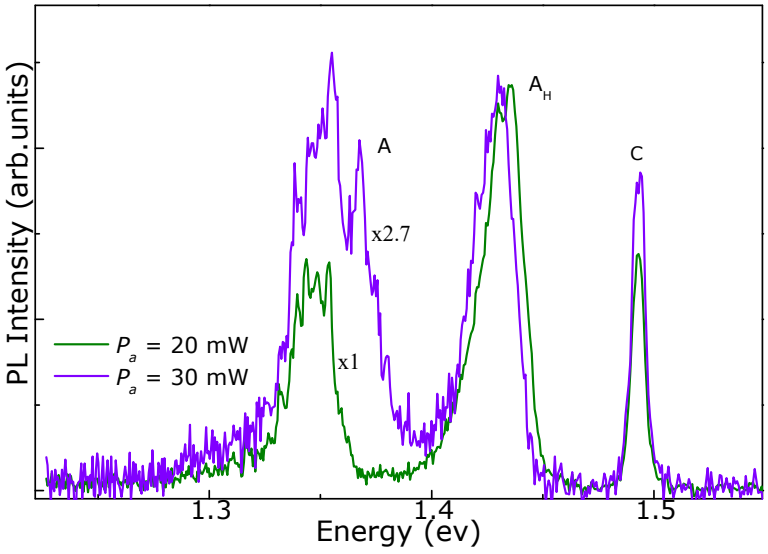

Figure 6.4: μPL spectra of the laser annealed spots in sample H2 (λ = 515 nm, t_a = 15 s, P_a = 20 and 30 mW).

As shown in Figure 6.4, band A becomes wider with increasing the power of the laser annealing from 20 to 30 mW. It can be seen that new and more intense N-related sharp emission lines appears in the laser annealed spot at P_a = 30 mW. Also, for larger P_a band A_H slightly red shifts towards band A.

6.3 Temperature dependent photoluminescence studies

In this section, we consider the temperature dependence of the QW PL emission. For this study, we used an experimental set up different from that described early for μPL experiments. In the μPL set up the sample is cooled down by direct contact with a cold metal surface in the cryostat. This cooling method is not always very effective, particularly for temperature dependent studies. Hence we use a set up in which the sample is mounted inside a cryostat and cooled by a continuous flux of helium surrounding the sample. A temperature meter and heater mounted close to the sample allowed us to control easily the sample temperature from 4.2 K to 300 K. An He-Ne laser beam (λ = 633 nm) with a power density of about 50 W/cm^2 was focused onto the sample by a lens with a focal length of 5 cm, thus providing a laser spot with diameter of ~ 100 μm. The emitted light from the sample was collected by the same lens and then focused by a second lens into the entrance slit of a 0.5m spectrometer equipped with a liquid–nitrogen cooled Si CCD photodetector (see Section 3.4). Figure 6.5 shows the PL spectra of sample H1 at various temperatures in the range 4.2 K – 290 K.

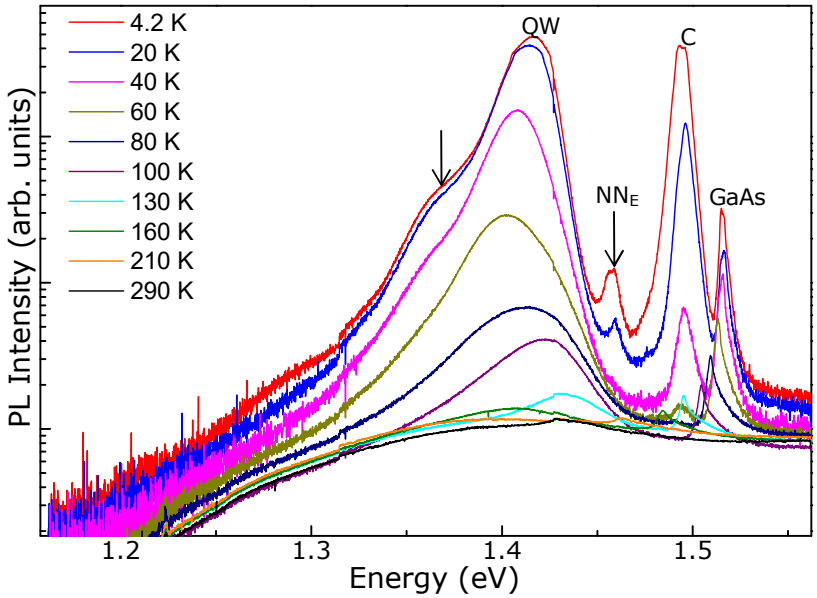

Figure 6.5: PL spectra of sample H1 at various temperatures.

It can be seen that the intensity of the PL emission continuously decreases with increasing temperature. We can identify the PL peaks corresponding to the GaAs free exciton (FE), the C-acceptor related transition at ~ 1.49 eV [68], the NN_E at ~ 1.46 eV [34, 68] and the Ga(AsN) QW emission. Also, a broad band at ~ 1.36 eV can be identified on the low energy side of the QW emission at low T and tends to quench at $T > 40$ K. This lower energy band was attributed before to N-related localized transitions [71]. The N-related transition NN_E tends to vanish at $T > 20$ K and the C-related transition quench at $T > 60$ K.

The QW PL peak energy shows a non-monotonic (red-blue-red) shift with increasing temperature, see Figure 6.6a. In contrast, the energy position of the GaAs PL peak shows a monotonic red shift with increasing temperature (see Figure 6.6b).

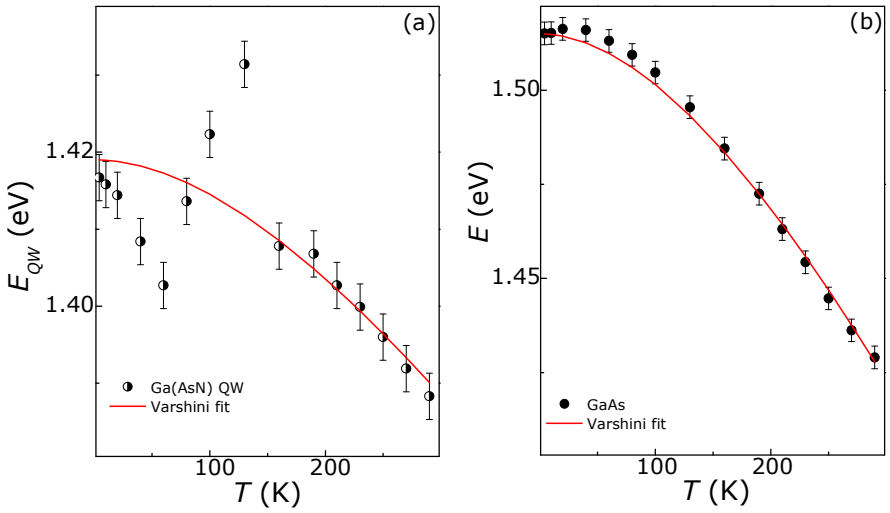

Figure 6.6: Dependence of the PL peak energy on temperature for (a) the Ga(AsN) QW and (b) GaAs. Solid lines are fits to the data by Varshni law.

The S-like shape of the QW PL peak energy versus temperature is attributed to the compositional alloy disorder and carrier thermal distribution effects. At low temperature, when excitons have not sufficient thermal energy to overcome potential energy barriers, they get trapped in local energy minima [26, 29]. This phenomenon called exciton freeze-out is illustrated in Figure 6.7a. With increasing temperature the excitons gain enough energy to overcome potential barriers and diffuse to neighbouring lower energy states (see Figure 6.7b). This redistribution of carriers can explain the red shift of the QW emission in the temperature range 4.2 K to 80 K. When the excitons gain adequate thermal energy to be excited to higher energy states, the QW PL emission blue shifts (80 K< T < 160 K). At about 160 K, the excitons become delocalized and the energy of QW PL emission tends to decrease with increasing temperature due to the band gap reduction [29]. The later effect is described by the Varshni equation

$$E_g(T) = E_g(0\ \text{K}) - \frac{\alpha T^2}{T+\beta}, \tag{2.10}$$

where $E_g(0\ \text{K})$ is the band gap at $T = 0$ K, and α and β are fitting parameters [28], see Table 6.1. The blue shift of the QW PL peak in our hydrogenated Ga(AsN) QW (~ 29 meV) is much larger than that reported for Ga(AsN)/GaAs (~ 10 meV) [72], and GaAsSbN/GaAs (~ 18 meV) [29] QWs. This might be caused by the larger disorder introduced by hydrogen.

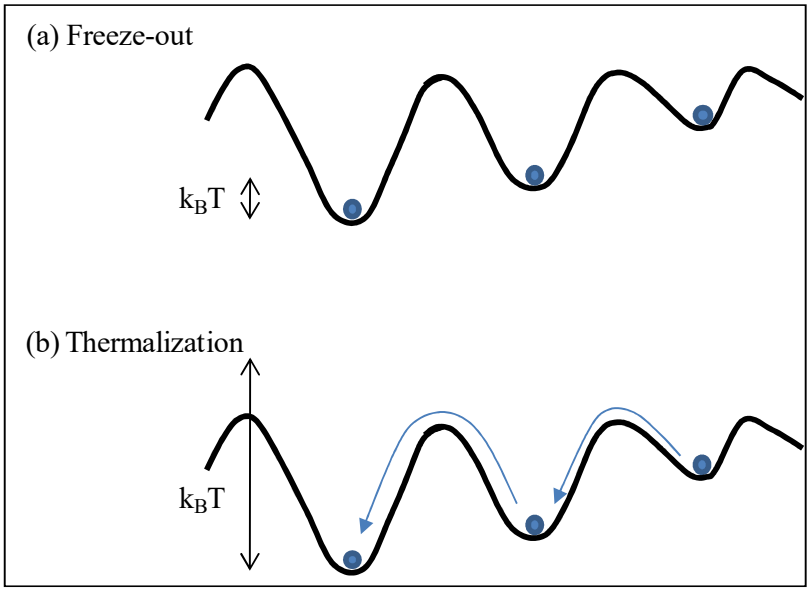

Figure 6.7: Schematic diagram of (a) exciton freeze-out and (b) thermal redistribution in a disordered potential.

Table 6.1: Parameters of Varshni equation for the temperature dependence of the PL peak energy for the Ga(AsN) QW and GaAs.

Solid Line	$E_g(T = 0\ \text{K})$ (eV)	α (x 10^{-4} eV/K)	β (K)
Varshni fit for Ga(AsN) QW	1.419	2.8	525
Varshni fit for GaAs	1.515	8.5	531

Chapter 7

Conclusion and Future Directions

The aim of this dissertation was to study the effect of a focussed laser beam on the electronic activity of N- and H-atoms in GaAs. The incorporation of a small concentration (~1%) of N-atoms in GaAs leads to a large reduction of the band gap energy [16]. On the other hand, the incorporation of hydrogen in Ga(AsN) acts to neutralize the electronic activity of N through the formation of H-N-H complexes with C_{1h} symmetry or C_{2v} asymmetry, thus reversing the effect of the N-atoms on the band structure of the host crystal [9, 43-44]. In this study, we used a focussed laser beam to control the electronic activity of N- and H-atoms in a Ga(AsN)/GaAs quantum well (QW). Our laser writing technique and micro-photoluminescence (μPL) studies provided real-time *in-situ* characterisation and control of the N-H complex dissociation and of the band gap energy of Ga(AsN).

We have shown that a focussed laser beam can be used to control spatially the PL emission energy of an hydrogenated Ga(AsN) quantum well. Also, our laser annealing studies have shown that the activation energy (E_a < 1 eV) and temperature (T_a ~ 100 °C) required for the N-H complex dissociation are significantly smaller than those obtained by HRXRD measurements of the lattice parameter during *in-situ* thermal annealing (E_a ~ 2 eV, T_a = 250-300 °C) [10]. Hence we have concluded that the N-H complex dissociation by laser arises from the combination of heating and photoexcitation phenomena. Our

laser writing technique provides an alternative method for H-defect engineering and for controlling the energy band gap and the confining potential of a QW of interest for future nanotechnologies. Additional studies are now required to model and probe the laser power and λ-dependence of the photodissociation of the N-H complex and to reveal clearly the role of thermal and photonic effects in the N-H dissociation.

We assessed the thermal stability of the laser-induced nanoscale light emitting spots by thermal annealing at temperatures T_a = 100-450 $^{\circ}$C and annealing time t_a = 1 hr. We have shown that the size of the spots remain constant up to $T_a \sim 200$ $^{\circ}$C. Also, the μPL measurements on the laser annealed spot after each thermal annealing allowed us to develop a simple model for the N-H complex dissociation. The laser annealing dissociates the N-H complexes and the H-atoms move to nearest interstitial positions inside or outside the spot without binding to the N-atoms. Thermal annealing at $T_a \sim 200$ °C facilitates the formation of the N-H complexes due to diffusion of H from these interstitial positions. At $T_a > 200$ $^{\circ}$C, the N-H complex dissociates and the laser annealed spots disappear due to a uniform out-diffusion of H. We find that the activation energy and temperature for thermal dissociation of the N-H complex (E_a = 1.6 eV and $T_a \sim 200$ ^{o}C) is comparable to those obtained by HRXRD measurements of the lattice parameter during *in-situ* thermal annealing [10]. This result again confirmed that the thermal dissociation of the N-H complex requires a significantly larger activation energy and temperature than those obtained by laser.

To probe the H-distribution profile across the laser annealed region, we performed SEM studies. We have shown that the H-profile inside the annealed region corresponds to an inverted Gaussian with a minimum due to a low H-concentration at the centre of the region. We have modelled the H-distribution profile using the Fick's equation for H diffusion in one dimension. Our model fits well the measured H-distribution profile. Also, we have shown that electron writing does not dissociate the N-H complexes. Further studies are now required to image the precise position of the diffused H-atoms following the laser annealing. This could be possible by *in-situ* focused ion beam (FIB) sample slicing and imaging by the FIB-SEM system or by transmission electron microscopy (TEM) [73].

We have indentified N-related states in hydrogenated and non-hydrogenated samples from the sharp lines of the low temperature PL spectra. The QW PL emission consists of several sharp lines at low temperature ($T \sim 5$ K) due to the recombination of exciton localized in local minima of the disordered QW potential caused by alloy disorder. In particular, the low energy tail can be accounted for by alloy compositional fluctuations. These tend to give rise to an exponential density of localized states thus resulting in broad and asymmetric PL line shapes. The temperature dependence of the QW PL peak energy also showed an S-shaped behaviour caused by carrier localization effects.

In conclusion, laser writing of the electronic activity of H-atoms in GaAs and other III-Vs could open up interesting possibilities for low-cost and high-speed nanofabrication techniques in nanophotonics. In particular, UV laser

writing and/or near-field laser irradiation [74] will help to gain further spatial control and resolution of the optical properties, which in our experiment is limited to ~ 0.8 μm for laser wavelengths of λ ~ 600 nm. These are exciting prospects for future studies of the electronic activity of H-atoms in III-Vs and its exploitation in optoelectronics.

Appendix A

Electron Effective Mass in $GaAs_{1-x}N_x$

The N-induced changes in the energy band gap of GaAs tend to modify the curvature of the energy–wave vector $E(k)$ dispersion of the CB, thus changing the electron effective mass m^*, which is defined as

$$m^*(k) = \frac{\hbar^2}{d^2E(k)/dk^2}. \tag{A.1}$$

According to the BAC model, the k-dependence of the $E_-(k)$ subband is

$$E_-(k) = \frac{1}{2}\left\{\left(E_N + E_M(k)\right) - \sqrt{\left[\left(E_N - E_M(k)\right)^2 + 4{C_{MN}}^2 x\right]}\right\}, \tag{A.2}$$

where $E_M(k)$ and E_N are, respectively, the energies of the GaAs CB host matrix and the N level measured with respect to the top of the valence band (VB), C_{MN} is a constant dependent on the host matrix, and x is the mole fraction of substitutional N.

The first derivative with respect to k of $E(k)$ is

$$\frac{dE_-(k)}{dk} = \frac{1}{2}\frac{dE_M(k)}{dk}\left[1 - \frac{\left(E_N - E_M(k)\right)}{\sqrt{\left(E_N - E_M(k)\right)^2 + 4{C_{MN}}^2 x}}\right]. \tag{A.3}$$

The second derivative with respect to k of $E(k)$ is

$$\frac{d^2E_-(k)}{dk^2} = \frac{1}{2}\frac{d^2E_M(k)}{dk^2}\left[1 - \frac{\left(E_N - E_M(k)\right)}{\sqrt{\left(E_N - E_M(k)\right)^2 + 4{C_{MN}}^2 x}}\right] + \frac{1}{2}\frac{dE_M(k)}{dk}\frac{d}{dk}\left(1 - \frac{\left(E_N - E_M(k)\right)}{\sqrt{\left(E_N - E_M(k)\right)^2 + 4{C_{MN}}^2 x}}\right). \tag{A.4}$$

At $k = 0$, $\frac{dE_-(k)}{dk} = 0$ and $\frac{dE_M(k)}{dk} = 0$. Thus we can write

$$\left.\frac{d^2E_-(k)}{dk^2}\right|_{k=0} = \left.\frac{d^2E_M(k)}{dk^2}\right|_{k=0}\left[1-\frac{\left(E_N-E_M(k)\right)}{\sqrt{\left(E_N-E_M(k)\right)^2+4C_{MN}{}^2\,x}}\right]_{k=0}. \tag{A.5}$$

Equation A.5 can also be written as

$$\frac{\hbar^2}{m^*} = \frac{1}{2}\,\frac{\hbar^2}{m_0^*}\left[1-\frac{\left(E_N-E_M(k)\right)}{\sqrt{\left(E_N-E_M(k)\right)^2+4C_{MN}{}^2\,x}}\right], \tag{A.6}$$

where m_0^* is the electron effective mass of GaAs at $k = 0$. Hence, the effective mass at $k = 0$ in Ga(AsN) can be written as

$$m^* = \frac{2m_0^*}{\left[1-\frac{\left(E_N-E_M(k)\right)}{\sqrt{\left(E_N-E_M(k)\right)^2+4C_{MN}{}^2\,x}}\right]}. \tag{A.7}$$

Appendix B

$GaAs_{1-x}N_x/GaAs$ Quantum Wells

Here we describe the electronic bound states of a Ga(AsN)/GaAs QW using the BAC model and a QW square potential model. The height of the QW is $V_0 = E_g(GaAs) - E_g(GaAs_{1-x}N_x)$ where E_g is the band gap energy. The potential profile along the z-direction is given by

$$V(z) = \begin{cases} V_0 & |z| > \frac{a}{2} \\ 0 & |z| < \frac{a}{2} \end{cases}, \tag{B.1}$$

where a is the width of the QW.

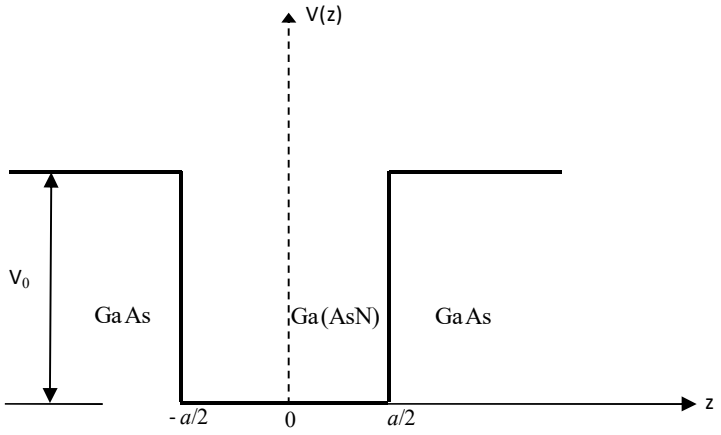

Figure B.1: Schematic diagram of a finite square Ga(AsN)/GaAs QW.

The wave functions inside the well have even/odd symmetry and can be written as $\psi(z) = C\begin{cases}\cos kz \\ \sin kz\end{cases}$, where $\varepsilon = \frac{\hbar^2 k^2}{2m_w^*}$ and m_w^* is the electron effective mass

inside the well. Outside the well, the time-independent Schrödinger equation can be written as

$$-\frac{\hbar^2}{2m_b^*}\frac{d^2}{dz^2}\psi(\mathrm{z}) + \mathrm{V}_0\psi(\mathrm{z}) = \varepsilon\psi(\mathrm{z}), \tag{B.2}$$

where $\varepsilon < \mathrm{V}_0$ and m_b^* is the electron effective mass outside the well. The solutions of Eq. B.2 are

$$\psi(\mathrm{z}) = D\exp(\pm K\mathrm{z}) \tag{B.3}$$

with

$$\frac{\hbar^2K^2}{2m_b^*} = \mathrm{V}_0 - \varepsilon. \tag{B.4}$$

Using boundary conditions at $\mathrm{z} = \frac{a}{2}$ and the continuity of $\psi(\mathrm{z})$, we obtain

$$\psi\left(\frac{\mathrm{a}}{2}\right) = C\begin{pmatrix}\cos\frac{ka}{2}\\ \sin\frac{ka}{2}\end{pmatrix} = D\exp\left(-\frac{1}{2}Ka\right). \tag{B.5}$$

Similarly, the continuity of the first derivative of ψ at $\mathrm{z} = \frac{a}{2}$ gives

$$\left.\frac{\mathrm{d}\psi}{\mathrm{dz}}\right|_{\mathrm{z}=\frac{a}{2}} = \frac{Ck}{m_w^*}\begin{pmatrix}-\sin\frac{ka}{2}\\ \cos\frac{ka}{2}\end{pmatrix} = -\frac{DK}{m_b^*}\exp\left(-\frac{1}{2}Ka\right). \tag{B.6}$$

Dividing Eq. B.5 and Eq. B.6 to eliminate the normalization factors *C* and *D*, we derive

$$\frac{k}{m_w^*}\begin{pmatrix}\tan\frac{ka}{2}\\ -\cot\frac{ka}{2}\end{pmatrix} = \frac{K}{m_b^*} \tag{B.7}$$

and

$$\begin{pmatrix}\tan\frac{ka}{2}\\ -\cot\frac{ka}{2}\end{pmatrix} = \frac{m_w^*K}{m_b^*k} = \frac{m_w^*}{m_b^*k}\sqrt{\frac{2m_b^*(\mathrm{V}_0-\varepsilon)}{\hbar^2}} = \sqrt{\frac{m_w^*}{m_b^*}\left(\frac{2m_w^*V_0}{\hbar^2k^2}-1\right)}. \tag{B.8}$$

We define $\theta = \frac{ka}{2}$ and

$$\theta_0{}^2 = \frac{m_w^*\mathrm{V}_0a^2}{2\hbar^2}. \tag{B.9}$$

Thus we can write

$$\begin{pmatrix} \tan\theta \\ -\cot\theta \end{pmatrix} = \sqrt{\frac{m_w^*}{m_b^*}\left(\frac{\theta_0{}^2}{\theta^2} - 1\right)}. \tag{B.10}$$

The parameter θ_0 determines the allowed values of θ. Both sides of Eq. B.10 are plotted against θ and the intersections give the solutions of θ.

The ground state energy ε_1

$$\varepsilon_1 = \frac{\hbar^2 k^2}{2m_w^*} = \frac{2\hbar^2\theta_1^2}{m_w^* a^2}, \tag{B.11}$$

corresponds to the first intersection point at $\theta = \theta_1$.

The energy of the optical transition between the first QW electron subband and the top of the valance band is

$$E_{QW} = E_g + \varepsilon_1, \tag{B.13}$$

where E_g is the band gap energy of $GaAs_{1-x}N_x$. Therefore, the modified BAC model for the QW is

$$E_{\pm}(k) = \frac{1}{2}\left\{(E_N + E_M(k) + \varepsilon_1) \pm \sqrt{\left[(E_N - E_M(k) - \varepsilon_1)^2 + 4C_{MN}{}^2 x\right]}\right\}.$$

Bibliography

[1] W. Shan, W. Walukiewicz, J.W. Ager III, E.E. Haller, J.F. Geisz, D.J. Friedman, J.M. Olson, and S.R. Kurtz, *Phys. Rev. Lett*. **82**, 1221 (1999).

[2] A. Lindsay and E.P. O'Reilly, *Phys. Rev. Lett*. **93**, 196402 (2004).

[3] J. Chevallier and M. Aucouturier, *Ann. Rev. Mater. Sci*. **18**, 219 (1988).

[4] C.G. Van de Walle and J. Neugebauer, *Nature* **423**, 626 (2003).

[5] G. Ciatto, F. Boscherini, A. Amore Bonapasta, F. Filippone, A. Polimeni, and M. Capizzi, *Phys. Rev. B* **71**, 201301(R) (2005).

[6] L. Wen, F. Bekisli, M. Stavola, W.B. Fowler, R. Trotta, A. Polimeni, M. Capizzi, S. Rubini, and F. Martelli, *Phys. Rev. B* **81**, 233201 (2010).

[7] M. Felici, A. Polimeni, G. Salviati, L. Lazzarini, N. Armani, F. Masia, M. Capizzi, F. Martelli, M. Lazzarino, G. Bais, M. Piccin, S. Rubini, and A. Franciosi, *Adv. Mater*. **18**, 1993-1997 (2006).

[8] M. Bissiri, G. Baldassarri H.v.H, A. Polimeni, M. Capizzi, D. Gollub, M. Fischer, M. Reinhardt, and A. Forchel, *Phys. Rev. B* **66**, 033311 (2002).

[9] M. Berti, G. Bisognin, D. De Salvador, E. Napolitani, S. Vangelista, A. Polimeni, M. Capizzi, F. Boscherini, G. Ciatto, S. Rubini, F. Martelli, and A. Franciosi, *Phys. Rev. B* **76**, 205323 (2007).

[10] G. Bisognin, D. De Salvador, E. Napolitani, M. Berti, A. Polimeni, M. Capizzi, S. Rubini, F. Martelli and A. Franciosi. *J. Appl. Cryst*. **41**, 366-372 (2008).

[11] R. Trotta, A. Polimeni, F. Martelli, G. Pettinari, M. Capizzi, L. Felisari, S. Rubini, M. Francardi, A. Gerardino, P.C.M. Christianen, and J.C. Maan, *Adv. Mater*. **23**, 2706-2710 (2011).

[12] T.C. Chong, M.H. Hong, and L.P. Shi, *Laser & Photonics Reviews* **4**, 123-143 (2010).

[13] N. López, L.A. Reichertz, K.M. Yu, K. Campman, and W. Walukiewicz, *Phys. Rev. Lett*. **106**, 028701 (2011).

[14] J.C. Fan, W.K. Hung, Y.F. Chen, J.S. Wang and H. H. Lin, *Phys. Rev. B* **62**, 10990 (2000).

[15] J. Wu, W. Shan and W. Walukiewicz, *Semicond. Sci. Technol*. **17**, 860-869 (2002).

[16] D.N. Talwar, *International Conference on Emerging Trends in Electronic and Photonic Devices & Systems (ELECTRO-2009),* 24 (2009).

[17] J.F. Geisz, D.J. Friedman, J.M. Olson, S.R. Kurtz, B.M. Keyes, *J. Cryst. Growth.* **195**, 401-408 (1998).

[18] C. Skierbiszewski, P. Perlin, P. Wisniewski, W. Knap, T. Suski, W. Walukiewicz, W. Shan, K.M. Yu, J.W. Ager, E.E. Haller, J.F. Geisz and J.M. Olson, *Appl. Phys. Lett.* **76**, 2409 (2000).

[19] M. Weyers, M. Sato and H. Ando, *Jpn. J. Appl. Phys.* **31**, L 853-L 855 (1992).

[20] S.Wei and A. Zunger, *Phys. Rev. Lett*. **76**, 664 (1996).

[21] K.M. Yu, W. Walukiewicz, W. Shan, J. W. Ager III, J. Wu, and E. E. Haller, *Phys. Rev. B* **61**, R13337 (2000).

[22] W. Walukiewicz, W. Shan, J.W. Ager III, D.R. Chamberlin, E.E. Haller, J.F. Geisz, D.J. Friedman, J.M. Olson, and S.R. Kurtz, *NREL/CP*-**520**, 29583 (1999).

[23] I. Vurgaftman and J.R. Meyer, *J. Appl. Phys*. **94**, 3675 (2003).

[24] M. Seifikar, E.P. O'Reilly, and S. Fahy, *Phys. Status Solidi B,* 1-4 (2011).

[25] O. Madelung, *Semiconductors: Data Handbook*. (3), Springer, 118 (2003).

[26] A. Bell, S. Srinivasan, C. Plumlee, H. Omiya, F.A. Ponce, J. Christen, S. Tanaka, A. Fujioka, and Y. Nakagawa, *J. Appl. Phys* **95**, 4670 (2004).

[27] J. Christen and D. Bimberg, *Phys. Rev. B* **42**, 7213 (1990).

[28] Y.P. Varshni, *Physica,* **34**, 149 (1967).

[29] J. Li, S. Iyer, S. Bharatan, L. Wu, K. Nunna, W. Collis, K.K. Bajaj and K. Matney, *J. Appl. Phys* **98**, 013703 (2005).

[30] D. Ouadjaout and Y. Marfaing, *Phys. Rev. B* **41**, 12096 (1990).

[31] A. Aït-Ouali, A. Chennouf, R.Y.-F. Yip, J.L. Brebner, R. Leonelli, and R.A. Masut, *J. Appl. Phys* **84**, 5639 (1998).

[32] A. Polimeni, M. Capizzi, M. Geddo, M. Fischer, M. Reinhardt, and A. Forchel, *Appl. Phys. Lett* **77**, 2870 (2000).

[33] P. R.C. Kent and A. Zunger, *Phys. Rev. B* **64**, 115208 (2001).

[34] T. Makimoto, H. Saito, and N. Kobayashi, *Jpn. J. Appl. Phy.* **36**, 1694-1697 (1997).

[35] G. Baldassarri H.v.H, M. Bissiri, A. Polimeni, M. Capizzi, M. Fischer, M. Reinhardt, and A. Forchel, *Appl. Phys. Lett* **78**, 3472 (2001).

[36] A. Polimeni, G. Ciatto, L. Ortega, F. Jiang, F. Boscherini, F. Filippone, A. Amore Bonapasta, M. Stavola, and M. Capizzi, *Phys. Rev. B* **68**, 085204 (2003).

[37] P.J. Klar, H. Grüning, M. Güngerich, W. Heimbrodt, J. Koch, T. Torunski, W. Stolz, A. Polimeni, and M. Capizzi, *Phys. Rev. B* **67**, 121206(R) (2003).

[38] A. Amore Bonapasta, F. Filippone, P. Giannozzi, M. Capizzi and A. Polimeni, *Phys. Rev. Lett*. **89**, 216401 (2002).

[39] A. Janotti, S. B. Zhang, Su-Huai Wei, and C. G. Van de Walle, *Phys. Rev. Lett*. **89**, 086403 (2002).

[40] Y. Kim and K.J. Chang, *Phys. Rev. B* **66**, 073313 (2002).

[41] F. Jiang, M. Stavola, M. Capizzi, A. Polimeni, A. Amore Bonapasta and F. Filippone, *Phys. Rev. B* **69**, 041309(R) (2004).

[42] S. Kleekajai, F. Jiang, K. Colon, M. Stavola, W.B. Fowler, K.R. Martin, A. Polimeni, M. Capizzi, Y.G. Hong, H.P. Xin, and C.W. Tu, G. Bais, S. Rubini, and F. Martelli, *Phys. Rev. B* **77**, 085213 (2008).

[43] A. Amore Bonapasta, F. Filippone and G. Mattioli, *Physics of Semiconductors, 28th International Conference*, 233 (2007).

[44] R. Trotta, A. Polimeni, and M. Capizzi, *Phys. Status Solidi C*. **6**, 2644-2648 (2009).

[45] HR800 user manual, Horiba Jobin Yvon.

[46] wiki.brown.edu/confluence/download/attachments/74853194/confocal+microscopy.png?version=1&modificationDate=1291661192000

[47] Advanced Research System, Inc. **www.arscyo.com**.

[48] TRIAX SERIES, JY JOBIN YVON. www.jyhoriba.com.

[49] Research Instruments, Operator's Handbook, OXFORD.

[50] www4.nau.edu/microanalysis/Microprobe-SEM/Instrumentation.html, © James H. Wittke, 2008.

[51] www.iap.tuwien.ac.at/www/atomic/instrumentation/uhv-afm

[52] R. Tsu, J.E. Baglin, G.J. Lasher, and J.C. Tsang, *Appl. Phys. Lett*. **34**, 153 (1979).

[53] C.T. Foxon, J.A. Harvey, and B.A. Joyce, *J. Phys. Chem. Solid.* **34** 1693-1701 (1973).

[54] M. Lax, *J. Appl. Phys*. **48**, 3919 (1977).

[55] J.S. Blakemore, *J. Appl. Phys*. **53**, R123 (1982).

[56] P.V. Santos, N.M. Johnson, and R.A. Street, *Phys. Rev. Lett*. **67**, 2686 (1991).

[57] D. Loridant-Bernard, S. Mezière, M. Constant, N. Dupuy, B. Sombret, and J. Chevallier, *Appl. Phys. Lett*. **73**, 644 (1998).

[58] B.L. Thiel and M. Toth, *J. Appl. Phys*. **97**, 051101 (2005).

[59] L. Felisari, V. Grillo, F. Martelli, R. Trotta, A. Polimeni, M. Capizzi, F. Jabeen, and L. Mariucci, *Appl. Phys. Lett.* **93**, 102116 (2008).

[60] M. Geddo, T. Ciabattoni, G. Guizzetti, M. Galli, M. Patrini, A. Polimeni, R. Trotta, M. Capizzi, G. Bais, M. Piccin, S. Rubini, F. Martelli, and A. Franciosi, *Appl. Phys. Lett*. **90**, 091907 (2007).

[61] D.D. Perovic, M.R. Castell, A. Howie, C. Lavoie, T. Tiedje, and J.S.W. Cole, *Ultramicroscopy* **58**, 104-113 (1995).

[62] C.P. Sealy, M.R. Castell and P.R. Wilshaw, *Jap. Soc. Electron Microscopy* **49** (2), 311-321 (2000).

[63] K. Fukui, H. Onishi, and Y. Iwasawa, *Phys. Rev. Lett*. **79**, 4202 (1997).

[64] S.L. Elliott, R.F. Broom, and C.J. Humphreys, *J. Appl. Phys*. **91**, 9116 (2002).

[65] S.M. Sze, Physics of Semiconductor Devices. (2), *New York: John Wiley & sons*, 67 (1981).

[66] J. Cocle, R. Gauvin, P. Hovington, M. Lagacé, and C.D. Fuerst, *Microsc Microanal* **13**, 946 CD (2007).

[67] J. Goldstein, D. Newbury, D. Joy, C. Lyman, P. Echlin, E. Lifshin, L. Sawyer, and J. Michael, 'Scanning electron microscopy and X-ray microanalysis'. **1**(3), *Springer*, (2003).

[68] F. Bousbih, S. Ben Bouzid, R. Chtourou, and J.C. Harmand, *Appl. Surface Science* **226**, 41-44 (2004).

[69] T. Makimoto, H. Saito, T. Nishida, and N. Kobayashi, *Appl. Phys. Lett.* **70**, 2984 (1997).

[70] M. Bissiri, V. Gaspari, G. Baldassarri H.v.H, F. Ranalli, A. Polimeni, M. Capizzi, A. Frova, M. Fischer, M. Reinhardt, and A. Forchel, *Phys. Stat. Sol. (a)* **190**, 651-654 (2002).

[71] Z.Y. Xu, X.D. Luo, X.D. Yang, P.H. Tan, C.L. Yang, W.K. Ge, Y. Zhang, A. Mascarenhas, H.P. Xin, and C.W. Tu, *Mat. Res. Soc. Symp. Prov.* **798**, Y5.68.1 (2004).

[72] V.M. Ustinov, N.A. Cherkashin, N.A. Bert, A.F. Tsatsul'nikov, A.R. Kovsh, J. Wang, L. Wei, and J.Y. Chi, *Mat. Res. Soc. Symp. Proc* **692**, H1.10 (2002).

[73] D. Drobne, M. Milani, A. Zrimec, V. Leser and M. Berden Zrimec, *J. Microscopy*. **219**, 29-35 (2005).

[74] F. Intonti, V. Matarazzo, A. Nasir, O. Makarovsky, R. Campion, A. Patanè, S. Kumar, A. Rastelli, O. G. Schmidt, and M. Gurioli, *Appl. Phys. Lett*. **98**, 183102 (2011).